animal facility at the Research Center for Animal Life Science of our institution. The bedding was highly absorbent, free of materials toxic to humans and animals, and unpalatable to the animals. We provided sufficient bedding to keep the animals dry and unsoiled by feces and urine, the bedding did not interfere with the animals' drinking. All bedding was stored on pallets to avoid contact with the floor. The room temperature was controlled at 22°C ± 4. The relative humidity was controlled at 40%–70%. The rats received a diet of commercially available pellets and water ad libitum.

The animals were anesthetized with an ip injection of pentobarbital (40 mg/kg, Dai Nippon Sumitomo Pharma Co. Ltd., Tokyo, Japan). In six randomly selected rats from groups 1 and 2 (three rats/group) we placed a 1-cm sc incision to create a pocket in the right lower quadrant for neodymium magnets (0.3 Tesla, 1 × 1 × 0.5 cm, Niroku Seisakusho, Shiga, Japan). Another 6 rats from groups 3 and 4 (3 rats/group) served as the control; they received similar sc incisions but no magnets were placed (Table 1). After the operation, all rats were injected intramuscularly with enrofloxacin (2.5%, 1 mL; Baytril®, Bayer Healthcare Co. Ltd., Tokyo, Japan) once a day for three consecutive days. On the seventh postoperative day they were used for the therapy portion of our study.

DM-Cis accumulation experiment after ip administration

Four days after the ip injection of 1 mL saline (groups 2 and 4, 3 rats/group) or 1 mL DM-Cis (groups 1 and 3, three rats/group) into the left upper quadrant (Table 1) all rats were sacrificed with pentobarbital (400 mg/kg, ip; Dai Nippon Sumitomo Pharma Co.). The magnets were removed, rectus abdominis muscle tissue just under the pocket was harvested, fixed in 10% buffered formalin for 24 hours, and embedded in paraffin. A 4-μm-thick slice of a sagittal section relative to the magnets was deparaffinized and stained with hematoxylin and eosin (H and E) and Berlin blue for the detection of iron. The iron-stained area (um^2) was calculated using Image-Pro Plus (Media Cybernetics, MD, USA). We extracted blue-stained portions from the muscle tissues (threshold: red 0–110, green 0–250, blue 0–250), computed the blue-stained area in one view (X100), recorded the average of 5 view areas, and evaluated the area stained positively for iron. For statistical analysis we used Dr SPSS II for Windows (SPSS Japan Inc., Tokyo, Japan). Significant differences in the iron-stained areas among groups of rats were determined with Tukey's HSD test. A P value of <0.05 was considered to indicate a significant difference.

Table 1 Protocol of the DM-Cis accumulation experiment

Groups	Magneto flasking subcutaneously	Intraperitoneal injection of DM-Cis
1 (Magnet/ip)	+	+
2 (Magnet)	+	–
3 (ip)	–	+
4 (Control)	–	–

In vivo exothermic experiment

Four rats were injected ip with DM-Cis and magnets were placed sc (Table 1). After 24 hours the magnets were removed from the pockets and 18-gauge venula catheter needles were inserted into the rectus abdominis muscle tissue just under the pocket to fix the thermometer (FL-2000; Anritsu Meter, Tokyo, Japan) at the target site. One thermometer was used to monitor the temperature in the rectus abdominis muscle tissue just under the pocket and another, inserted into the rectum, to monitor the rectal temperature. These rats were placed into the IH coil for temperature measurements.

Results

Size of DM-Cis

The diameter of the DM-Cis complex was 59.6 ± 0.4 nm (± mean standard deviation).

Platinum concentration in DM-Cis

Defining 1 mL DM to 1 mL Cis as a ratio of 1:1, the concentration of platinum at 1.0:0.05, 1.0:0.1, 1.0:0.5, and 1:1 (DM:Cis) was 11.66 ± 1.13, 17.54 ± 1.84, 80.83 ± 2.91, and 105.60 ± 9.03 ug/mL, respectively (Figure 2).

In vitro exothermic experiment using a magnetic field

Under the portable IH device, the DM-Cis (5 mL, DM:Cis = 1:1 (v:v) solution could be heated at a rate of 0.12°C/sec. The temperature rose to 60°C in approximately 5 min (Figure 3).

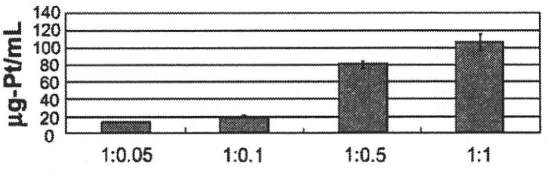

Figure 2 Conjugated concentration of platinum in the DM complex. Defining 1 mL DM to 1 ml Cis as a 1:1 ratio, this graph shows the concentration of platinum at 1.0:0.05, 1.0:0.1, 1.0:0.5, and 1:1 (DM:Cis). The platinum concentration at the applied concentrations of platinum conjugated with DM was 11.66 ± 1.13, 17.54 ± 1.84, 80.83 ± 2.91, and 105.60 ± 9.0 ug/mL, respectively.

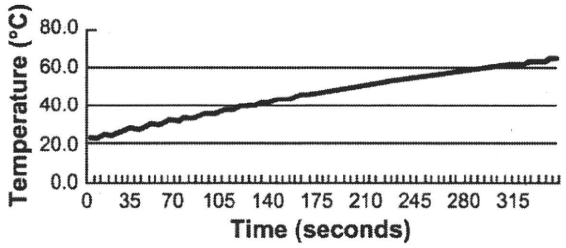

Figure 3 The temperature of DM-Cis under a portable IH device. Under the IH device, DM-Cis (5 mL, DM:Cis = 1:1) could be heated at a rate of 0.12°C/sec. The temperature was maintained at 60°C for 5 minutes.

Concentration and desorption of platinum from DM-Cis in bovine serum

Approximately 0.58, 1.20, 4.42, 9.30, 16.42, and 33.48% of platinum in DM-Cis was released at 30 min and at 1, 3, 6, 12, and 24 hours, respectively. The platinum concentration in the solution remaining in the dialysis tube was 65.32% of the total amount of platinum (Figure 4).

In vivo intraperitoneal accumulation

In group 1 we observed an extraordinary accumulation of DM-Cis in the peritoneum just under the magnet (Figure 5). There was no such accumulation in the other groups (data not shown). In addition, there was a significant difference between group 1 and the other groups with respect to the accumulation of DM-Cis in muscle tissues (Figure 6).

In vivo exothermic experiment

Figure 7 shows the individual temperature profiles in rectus abdominis muscle tissue just under the pocket and in rectal tissue. The temperature in muscle tissues was maintained at a maximum of 56°C after 4 minutes. The rectal temperature elevation was slight. No rats died from exposure to high heat or electromagnetic waves.

Discussion

We developed a DM-Cis complex that manifests hyperthermic effects and is manipulated magnetically in the abdominal cavity of rats and at elevated temperatures *in vivo* under the IH system.

The size of the DM-Cis complex was 59.6 ± 0.4 nm. As DM measures 55.7 nm, there was apparently no DM-Cis aggregation. While aggregates of this DM-Cis complex may not spread well in breast ducts, the size of the formed DM-Cis complex can be expected to remain stable.

When we reacted DM with Cis at a 1:1 ratio, the platinum concentration of DM-Cis (DM:Cis = 1:1) was 105.60 ± 9.03 ug/mL, approximately 32% of the platinum concentration in a pharmaceutical Cis preparation (Randa®, Nippon Kayaku Co. Ltd, Tokyo, Japan). The Cis concentration in DM-Cis is relatively high, rendering it clinically useful. Under the IH device, the temperature of DM-Cis *in vitro* rose to 60°C or more in approximately 5 min. At that temperature there are obvious hyperthermic effects. However, to be useful, Cis must be released from the DM-Cis complex. We found that in the

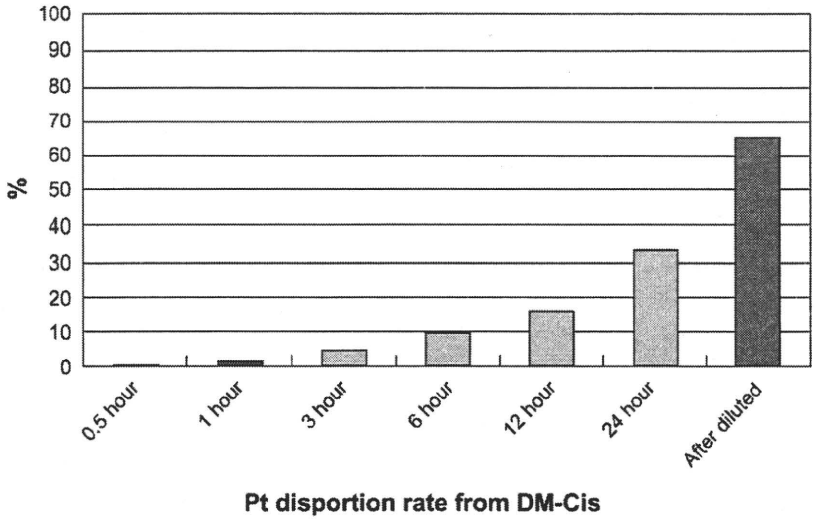

Figure 4 Time course of platinum release from DM-Cis in bovine serum. Approximately 0.58, 1.20, 4.42, 9.30, 16.42, and 33.48% of platinum in DM-Cis was released at 30 minutes and at 1, 3, 6, 12, and 24 hours, respectively.

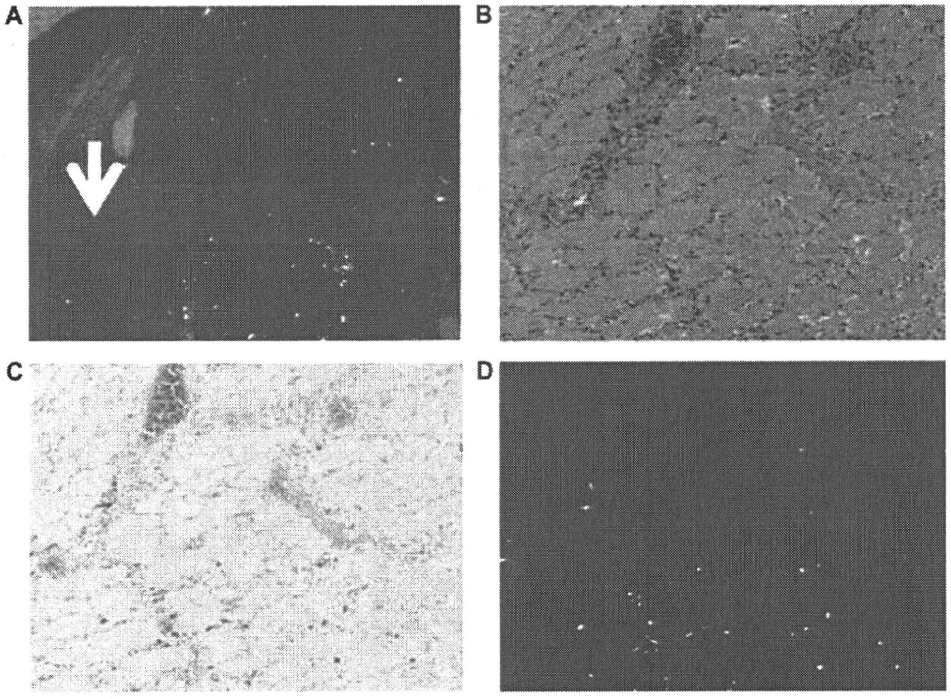

Figure 5 Accumulation of DM-Cis in group I rats. **a)** Macroscopic image of DM-Cis accumulation in the peritoneum. **b)** H & E stains (X100) of rectus abdominis muscle tissue just under the pocket harboring the magnets. Note the aggregation of phagocytes in muscle tissue. **c)** Berlin-blue stains (X100). Iron distributed in the muscle tissues is blue. **d)** Masked image using Image-Pro Plus. Only portions dyed blue are identified by white dots using Image-Pro Plus.

course of 24 hours, approximately 30% of Cis was desorbed in bovine serum, suggesting that the continued presence of Cis enhances its anti-tumor effects. In addition, DM-Cis accumulated in the rat peritoneum in a 0.3 Tesla magnetic field and as in muscle tissues just under the DM-Cis area, the iron concentration was clearly increased. It may be possible to trap DM-Cis for prolonged periods with a magnet in ducts and main tumor areas. The maximum temperature was 56°C and the area of hyperthermia was concentrated just beneath the *in vivo* DM-Cis accumulation site. For thermal treatment, temperatures of approximately 42°C are considered sufficient to induce anti-tumor effects.[14] A temperature rise to 56°C may coagulate targeted tissues directly.[15]

In one rat the temperature rose to 40.7°C in the rectus abdominis muscle tissue located just under the pocket. This raises the concern that some infused DM-Cis may be accidentally injected into sc tissue, resulting in a decrease in the total

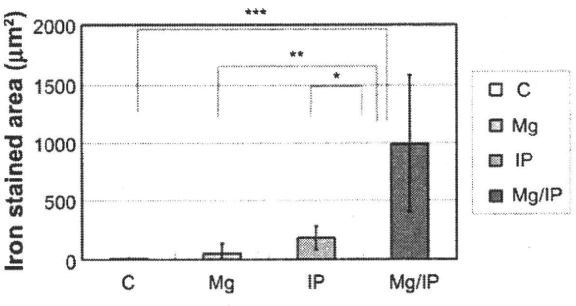

Figure 6 Total iron-stained area (μm²). Group I differed significantly from the other three groups with respect to the iron-stained area in muscle tissues ($P < 0.05^{*,**,***}$). There was no significant difference among groups 2, 3, and 4.

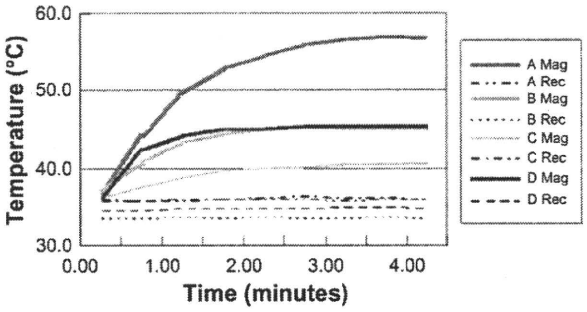

Figure 7 Temperature profiles of muscle and rectal tissues under the portable IH device. Group I rats (n = 4) were placed into the IH coil and the temperature was increased to 46.98 ± 7.0°C on average. The temperature in muscle tissues reached a maximum of 56°C after 4 min. The temperature increase in rectal tissue was slight. None of the experimental rats died from exposure to high heat or electromagnetic waves.

amount of DM-Cis accumulated in the peritoneum and a lowering of the heat value. In another three rats, the temperature rise was sufficient to achieve hyperthermic effects. Moreover, these temperature gains were produced within 5 minutes, but according to others,[6,7] the time required for similar temperature increases was longer. Our technique makes it possible to avoid raising the temperature in other parts of the body. None of our rats died during the heating procedure, suggesting the clinical applicability of this technique. Slow-release antitumor drugs with hyperthermic potential that can be magnetically manipulated and collected may be a more effective treatment of some cancers than surgical resection.

Our study has some limitations. Firstly, we did not compare the anti-tumor effects of DM-Cis *in vivo* and *in vitro*. Although Cis-conjugated gelatin maintained its anti-tumor effects *in vivo*,[13] we need to determine whether Cis-conjugated DM also retains these effects. Studies are underway in our laboratory to examine its effects in experimental mouse breast carcinoma. Secondly, we did not carry out ductal accumulation experiments. As ductal is slower than blood vessel flow, we posit that DM-Cis may fully accumulate magnetically. We are testing this hypothesis in a murine breast carcinoma model in which we administer DM-Cis via mammary ducts. Thirdly, we did not quantify the relationship between the concentration of accumulated iron and the distance between the site of accumulation and the site of temperature elevation. Our purpose in the current study was to examine whether DM-Cis can generate heat *in vivo* to the degree at which hyperthermia is induced. Fourthly, the long-term safety of DM-Cis remains to be established. However, as both DM and Cis are used clinically, these materials have been shown to be safe. We will perform additional experiments to address this issue. And finally, our study sample was deliberately small because our experiments to determine whether DM-Cis can generate heat *in vivo* exposed the animals to significant distress.

Disclosure

The authors report no conflicts of interest in this work.

References

1. Kopp AF, Laniado M, Dammann F, et al. MR imaging of the liver with Resovist: safety, efficacy, and pharmacodynamic properties. *Radiology*. 1997;204(3):749–756.
2. Kobeiter H, Georgiades CS, Leakakos T, et al. Targeted transarterial therapy of Vx-2 rabbit liver tumor with Yttrium-90 labeled ferromagnetic particles using an external magnetic field. *Anticancer Res*. 2007; 27(2):755–760.
3. Jordan A, Wust P, Fahling H, et al. Inductive heating of ferrimagnetic particles and magnetic fluids: physical evaluation of their potential for hyperthermia. *Int J Hyperthermia*. 1993;9(1):51–68.
4. Moroz P, Jones SK, Winter J, et al. Targeting liver tumors with hyperthermia: ferromagnetic embolization in a rabbit liver tumor model. *J Surg Oncol*. 2001;78(1):22–49; discussion 30–31.
5. Moroz P, Metcalf C, Gray BN. Histologic analysis of liver tissue following hepatic arterial infusion of ferromagnetic particles in a rabbit tumour model. *Biometals*. 2003;16(3):455–464.
6. Motoyama J, Yamashita N, Morino T, et al. Hyperthermic treatment of DMBA-induced rat mammary cancer using magnetic nanoparticles. *Biomagn Res Technol*. 2008;6:2.
7. Takamatsu S, Matsui O, Gabata T, et al. Selective induction hyperthermia following transcatheter arterial embolization with a mixture of nano-sized magnetic particles (ferucarbotran) and embolic materials: feasibility study in rabbits. *Radiat Med*. 2008;26(4):179–187.
8. Wada S, Yue L, Tazawa K, et al. New local hyperthermia using dextran magnetite complex (DM) for oral cavity: experimental study in normal hamster tongue. *Oral Dis*. 2001;7(3):192–195.
9. Mitsumori M, Hiraoka M, Shibata T, et al. Development of intra-arterial hyperthermia using a dextran-magnetite complex. *Int J Hyperthermia*. 1994;10(6):785–793.
10. Mitsumori M, Hiraoka M, Shibata T, et al. Targeted hyperthermia using dextran magnetite complex: a new treatment modality for liver tumors. *Hepatogastroenterology*. 1996;43(12):1431–1437.
11. Murata S, Kominsky SL, Vali M, et al. Ductal access for prevention and therapy of mammary tumors. *Cancer Res*. 2006;66(2):638–645.
12. Sonoda A, Nitta N, Ohta S, et al. Development of a conjugated gadolinium and cisplatin-gelatin possessing properties as an intravascular contrast agent for MR imaging. *Eur J Radiol*. 2009;71(3): 570–575.
13. Konishi M, Tabata Y, Kariya M, et al. In vivo anti-tumor effect of dual release of cisplatin and adriamycin from biodegradable gelatin hydrogel. *J Control Release*. 2005;103(1):7–19.
14. Hilger I, Hergt R, Kaiser WA. Use of magnetic nanoparticle heating in the treatment of breast cancer. *IEE Proc Nanobiotechnol*. 2005; 152(1):33–39.
15. Heisterkamp J, van Hillegersberg R, Ijzermans JN. Critical temperature and heating time for coagulation damage: implications for interstitial laser coagulation (ILC) of tumors. *Lasers Surg Med*. 1999;25(3): 257–262.

Laboratory Investigation (2011) 91, 262–272

Epidermal growth factor induces cytokeratin 19 expression accompanied by increased growth abilities in human hepatocellular carcinoma

Norihide Yoneda[1,2], Yasunori Sato[1], Azusa Kitao[1,2], Hiroko Ikeda[3], Seiko Sawada-Kitamura[3], Masami Miyakoshi[1], Kenichi Harada[1], Motoko Sasaki[1], Osamu Matsui[2] and Yasuni Nakanuma[1]

Cytokeratin (CK) 19-positive hepatocellular carcinoma (HCC) has been reported to have a poor prognosis. The mechanism of the development of CK19-positive HCC remains to be studied. To clarify this, *in vitro* experiments were performed using human HCC cell lines (PLC-5, HepG2), and the phenotypic changes after stimulation with several growth factors were examined using quantitative reverse transcriptase PCR, western blotting, and immunofluorescence staining. *In vivo* experiments using human HCC specimens obtained from a total of 78 patients and clinicopathological analysis were also performed. Among the growth factors tested, epidermal growth factor (EGF) had prominent effects on inducing CK19 expression in PLC-5 and HepG2, which was accompanied by the reduced expression of α-fetoprotein in PLC-5. The induction of CK19 expression after EGF stimulation was accompanied by the phosphorylation of c-Jun-N-terminal kinase (JNK)/stress-activated protein kinase, which was blocked by the addition of JNK inhibitors. EGF also increased proliferative abilities and invasive properties of the HCC cell lines. *In vivo*, 9 (12%) of 78 HCC cases showed positive immunohistochemical staining of CK19. The extent of positive immunhistochemical signals of EGF, EGF receptor (EGFR), and JNK expression was significantly intense in CK-19-positive HCC than those of CK19-negative HCC. Clinicopathological analysis showed that CK19-positive HCC had a high incidence of portal vein invasion, extrahepatic metastasis and an early relapse, which was associated with the worsened 2-year disease free survival. These results indicate that the activation of the EGF–EGFR signaling pathway is associated with the development of CK19-positive HCC, and the EGF-induced increase in growth abilities of HCC may account for the poor prognosis of the patients.
Laboratory Investigation (2011) **91**, 262–272; doi:10.1038/labinvest.2010.161; published online 20 September 2010

KEYWORDS: CK19-positive HCC; EGF; EGFR; histogenesis; prognosis

Hepatocellular carcinoma (HCC) is the fifth most important cancer worldwide, and is the third most common cause of death from cancer.[1] Its incidence and mortality rates have increased in recent years.[2] The high rate of recurrence or metastases after curative resection leads to worse prognosis in HCC.[3,4]

Recently, several authors have reported the positive immunoexpression of cytokeratin (CK) 19 in HCC, and CK19-positive HCC has been shown to have a high metastatic potential, which is associated with a poor prognosis.[5–10] The expression of CK19 in HCC is implicated as a novel predictor for the poor prognosis of the patients after curative resection.[8,11,12] Although the clinical significance of CK19-positive HCC seems to be establishing, the mechanism underlying the development of CK19-positive HCC remains to be unclear.

CK is cytoskeletal intermediate filaments, and different epithelial cells express characteristic combinations of CK polypeptides depending on the organ or on the type of differentiation.[13,14] In normal liver, hepatocytes express CK8 and CK18, and cholangiocytes express CK7 and CK19.[15,16] Bipotential hepatic progenitor cells have been shown to express CK7 and CK19.[17]

Previous studies showed that rat hepatocytes had a potential to differentiate into bile duct-like cells *in vitro*.[18–22] In these studies, epidermal growth factor (EGF) and hepatocytes growth factor (HGF) are potent inducers of biliary

[1]Department of Human Pathology, Kanazawa University Graduate School of Medicine, Kanazawa, Japan; [2]Department of Radiology, Kanazawa University Graduate School of Medicine, Kanazawa, Japan and [3]Division of Diagnostic Pathology, Kanazawa University Hospital, Kanazawa, Japan
Correspondence: Dr Y Nakanuma, MD, PhD, Department of Human Pathology, Kanazawa University Graduate School of Medicine, 13-1 Takara-machi, Kanazawa 920-8640, Japan. E-mail: pbcpsc@kenroku.kanazawa-u.ac.jp

Received 23 February 2010; revised 23 July 2010; accepted 9 August 2010

phenotype in rat hepatocytes.[18–22] Transforming growth factor-β1 (TGF-β1) and basic fibroblast growth factor (FGF-b) are also well-known growth factors that have key roles in the development and differentiation of the liver.[23–26] These observations suggest that the expression of CK19, one of the characters of biliary CK, may be induced in HCC after stimuli by a certain kind of growth factors, accounting for the development of CK19-positive HCC.

Understanding the developmental mechanism of CK19-positive HCC is particularly important, because it may lead to a novel therapeutic approach for the carcinoma with a poor prognosis. To clarify the histogenesis of CK19-positive HCC, this study was conducted using human HCC cell lines, and *in vivo* experiments using human HCC specimens and clinicopathological analysis were also performed.

MATERIALS AND METHODS

Cell Culture

Human HCC cell lines (PLC-5, HepG2) were purchased from the Health Science Research Resources Bank (Osaka, Japan), and were maintained with Dulbecco modified Eagle medium supplemented with 10% fetal bovine serum (FBS) and 1% antibiotics-antimycotic (all from Invitrogen, Carlsbad, CA, USA). Cells were incubated in 7.5% CO_2 at 37°C. The cells were treated with EGF (30 ng/ml), TGF-β1 (10 ng/ml), HGF (50 ng/ml), and FGF-b (50 ng/ml) for 5 days (all from R&D systems, Minneapolis, MN, USA). Treatment with growth factors was carried out with culture medium that did not contain FBS. To block the activity of c-Jun-N-terminal kinase (JNK), JNK inhibitor I (1 μM; Merck, Darmstadt, Germany) and JNK inhibitor II (50 nM; Merck) were used.

Reverse transcriptase PCR (RT-PCR) and Quantitative Real-Time PCR

RT-PCR was performed using total RNA (1 μg) extracted from the cells. Total RNA was extracted using an RNA extraction kit (RNeasy mini; Qiagen, Tokyo, Japan) and was used to synthesize cDNA with reverse transcriptase (ReverTra Ace; Toyobo, Osaka, Japan). The sequences of the primers and conditions for PCR used are shown in Table 1. The PCR products were subjected to 2% agarose gel electrophoresis and stained with ethidium bromide.

Quantitative real-time PCR was performed according to a standard protocol using the SYBR Green PCR Master Mix (Toyobo) and ABI Prism 7700 Sequence Detection System (PE Applied Biosystems, Warrington, UK). Cycling conditions were incubation at 50°C for 2 min, 95°C for 10 min, and 40 cycles of 95°C for 15 s and 60°C for 1 min. Fold difference compared with glyceraldehyde-3-phosphate dehydrogenase expression was calculated.

Western Blot Analysis

Total proteins were extracted from the cells using T-PER protein extraction reagent (Pierce Chemical, Rockford, IL, USA). The protein was subjected to 10% SDS-polyacrylamide electrophoresis, and then electrophoretically transferred on to a nitrocellulose membrane. The membrane was incubated with primary antibodies against CK19 (1:100, RCK108, mouse monoclonal; DakoCytomation, Glostrup, Denmark), α-fetoprotein (AFP; 1:500, rabbit polyclonal; DakoCytomation), EGF receptor (EGFR; 1:100, rabbit polyclonal; Santa Cruz Biotechnology, Santa Cruz, CA, USA), phospho-JNK/stress-activated protein kinase (SAPK; 1:1000, rabbit monoclonal), phospho-p38 mitogen-activated protein kinase (MAPK; 1:1000, rabbit monoclonal), phospho-p44/42 MAPK (extracellular signal-regulated kinase1/2, ERK1/2; 1:2000, rabbit monoclonal), phospho-Akt (1:2000, rabbit monoclonal; all from Cell Signaling Technology, Danvers, MA, USA), and actin (1:3000, AC-15, mouse monoclonal; Abcam, Cambridge, MA, USA). The protein expression was detected using an EnVision + system (DakoCytomation), and 3,3′-diaminobenzidine tetrahydrochloride (DAB) was used as the chromogen. Semiquantitative analysis of the results was performed using NIH J image software (National institutes of Health, Bethesda, MD, UAS). The fold difference compared with actin expression was calculated.

Table 1 Sequences of the primers and PCR conditions used in this study

Gene	Sequences (5′–3′)	Annealing temperature (°C)	PCR cycles	Product size (bp)
CK19	tcccgcgactacagccactactacacgacc	60	30	745
	cgcgacttgatgtccatgagccgctggta			
AFP	gggagcggctgacattatta	55	40	231
	tcttgcttcatcgtttgcag			
Vimentin	ctcggtggacttctcgctggcc	67	25	612
	tcctgcaggttcttggcagcc			
EGFR	cctttggggcatagatcaga	55	40	172
	gctgacctggagggaacata			
GAPDH	gagtcaacggatttggtcgt	55	30	240
	ttgattttggagggatctc			
CK19 Real-time PCR	ggtcagtgtggaggtggatt	60	40	198
	tcagtaacctcggacctgct			

Abbreviations: AFP, α-fetoprotein; CK, cytokeratin; EGFR, epidermal growth factor receptor; GAPDH, glyceraldehyde-3-phosphate dehydrogenase.

Immunofluorescence Staining

Cultured cells grown in a Lab-Tek chamber (Nalge Nunc International, Naperville, IL, USA) were assessed. Treatment with EGF (30 ng/ml) was performed for 5 days. The cells were fixed with 4% paraformaldehyde for 15 min and permeabilized for 3 min with 0.1% Triton X-100. After blocking, the cells were incubated overnight at 4°C with primary

antibodies against CK19 (1:100, DakoCytomation), and AFP (1:500, DakoCytomation). Color development was performed using the Vector Red alkaline phosphatase substrate kit (Vector Laboratories, Burlingame, CA, USA). Nuclei were stained with 4′6-diamino-2-phenylindole. The sections were observed under a fluorescence microscope. Negative controls were carried out by substitution of the primary antibodies with non-immunized serum.

WST1 Cell Proliferation Assay

The effects of EGF on cell proliferative activity were assessed using a WST1 assay (Roche Diagnostics KK, Indianapolis, IN, USA). The cells were seeded on 96 well dishes, and were incubated with standard medium for 24 h. After the pre-incubation, the medium was exchanged for that containing EGF (30 ng/ml), and the cells were further incubated at indicated intervals. Then, the WST1 reagent was added, and the cell proliferative activity was determined spectrometrically. Each experiment was conducted in five sets.

Invasion Assay

Invasion assays were performed using Bio-coat cell migration chambers (BD Biosciences, Bedford, MA, USA) according to the manufacturer's instructions. A total of 5×10^4 cells were seeded on cell culture inserts, and the effects of EGF (30 ng/ml) on the invasive properties was determined. After 72 h after EGF stimulation, the cells were fixed in 100% methanol, and stained with hematoxylin. Cells that had migrated to the bottom side of the membrane were visualized under the microscope, and quantified by counting the number of cells in six randomly chosen visual fields.

Liver Specimens

A total of 78 patients with HCC, in which curative surgical hepatectomy was performed, were surveyed. The diagnosis of HCC was confirmed by the clinical and radiological data, and the histology of resected specimens. In this study, combined hepatocellular cholangiocarcinoma was not included. Such cases as relapse, non-curative resection, having history of anticancer treatment before operation, having cancerous thrombi in the portal vein, and having extrahepatic metastasis at the time of operation were excluded for the analysis. Tumor staging was defined according to the sixth edition of tumor–node–metastasis classification of Unio Internationale Contra Cancrum. The follow-up period ranged from 6 to 60 months. The diagnosis of recurrence was made on the basis of typical imaging appearance. Patients who had recurrent tumor received further treatments such as hepatectomy, radiofrequency ablation, transcatheter arterial chemoembolization, or chemotherapy, in which the adaptation was determined based on each patient condition.

Immunohistochemistry

Immunostaining was performed using formalin-fixed, paraffin-embedded tissue sections of surgically resected liver specimens of 78 HCC patients. After blocking the endogenous peroxidase, the sections were incubated in protein block solution (DakoCytomation). For the immunostaining of CK19 and JNK, antigen retrieval was performed by microwaving in 10 mmol/l citrate buffer pH 6.0. The sections were incubated overnight at 4°C with primary antibodies against CK19 (1:100, DakoCytomation), EGF (1:50, goat polyclonal; Santa Cruz Biotechnology), and JNK (1:50, mouse monoclonal; Santa Cruz Biotechnology). Then the sections were incubated with secondary antibodies conjugated to peroxidase-labeled polymer, EnVision system (DakoCytomation) or Histofine Simple Stain MAX PO(G) (Nichirei, Tokyo, Japan). Color development was performed using DAB, and the sections were counterstained with hematoxylin. Negative controls were carried out by substitution of the primary antibodies with non-immunized serum, resulted in no signal detection.

Immunostaining of EGFR was performed using the commercially available kit, EGF pharmDx (DakoCytomation) according to manufacturer's instructions.

Double immunostaining of EGFR and CK19 was performed for the liver sections. First, immunostaining of EGFR was performed as above. After microwaving in 10 mmol/l citrate buffer pH 6.0 for 10 min, the sections were then incubated overnight at 4°C with the anti-CK19 antibody (1:100, DakoCytomation.). Color development was performed using the Vector Red alkaline phosphatase substrate kit (Vector Laboratories), and the sections were counterstained with hematoxylin.

Semiquantitative analysis of the results of immunostaining was performed for EGF, EGFR, and JNK. The results of immunostaining were categorized as follows: 1+, 1–10% positive; 2+, 11–50% positive; 3+, 51–100% positive.

In Situ Hybridization

Single-strand RNA probes for the EGFR were obtained by RT-PCR and *in vitro* transcription. Briefly, the T7- or SP6-RNA polymerase promoter was attached to primer. Then, single strand RNA probes complementary (antisense) and anticomplementary (sense) to the corresponding gene transcripts were obtained using *in vitro* transcription according to the standard protocol of the digoxigenin RNA transcription kit (Roche Diagnostics, Basel, Switzerland). The paraffin sections were incubated with hybridization solution (DakoCytomation) mixed with the digoxigenin-labeled antisense or sense probes at 50°C for 20 h. After washing, the sections were incubated with alkaline phosphatase-conjugated antidigoxigenin antibody (Roche Diagnostics) at room temperature for 1 h. Color development was performed with a nitroblue tetrazolium salt/5-bromo-4-chloro-3-indolyl phospate toluidine salt solution (Roche Diagnostics) for 1 h.

Statistics

The data were expressed as the mean ± s.d. Statistical significance was determined using the Mann–Whitney *U*-test. Cumulative survival time was calculated by the Kaplan–Meier

method and analyzed by the log-rank test. The relationship among CK19 immunoreactivity and clinicopathological parameters was analyzed using Mann-Whitney *U*-test and Chi square test. A *P*-value <0.05 was accepted as the level of statistical significance.

RESULTS

Expression Analysis Of CK19 mRNA after Growth Factor Stimulation in HCC Cell Line

At first, the effect of growth factor stimulation on CK19 mRNA expression was examined using a HCC cell line, PLC-5. PLC-5 was treated with EGF, TGF-β1, HGF, and FGF-b, and the expression of CK19 mRNA was examined using RT-PCR. Among the growth factors tested, EGF had a prominent effect on the induction of CK19 mRNA in PLC5, and the mRNA expression of AFP was reduced (Figure 1a). Treatment with HGF and FGF-b seemed to have little effects on the mRNA expression of CK19 and AFP, whereas TGF-β1 reduced CK19 and AFP mRNA expression (Figure 1a). TGF-β1 induced the mRNA expression of vimentin, a hall marker of mesenchymal cells, and the expression of vimentin mRNA was unchanged after stimulation with EGF, HGF, and FGF-b (Figure 1a).

On phase-contrast microscope, no morphological alteration was observed after treatment with EGF, HGF and FGF-b, whereas TGF-β1 induced spindle cell morphology, simulating the phenomenon of epithelial-to-mesenchymal transition (Figure 1b). On the basis of these results, we focused on the effects of EGF, and further *in vitro* analysis was performed using two HCC cell lines (PLC-5, HepG2).

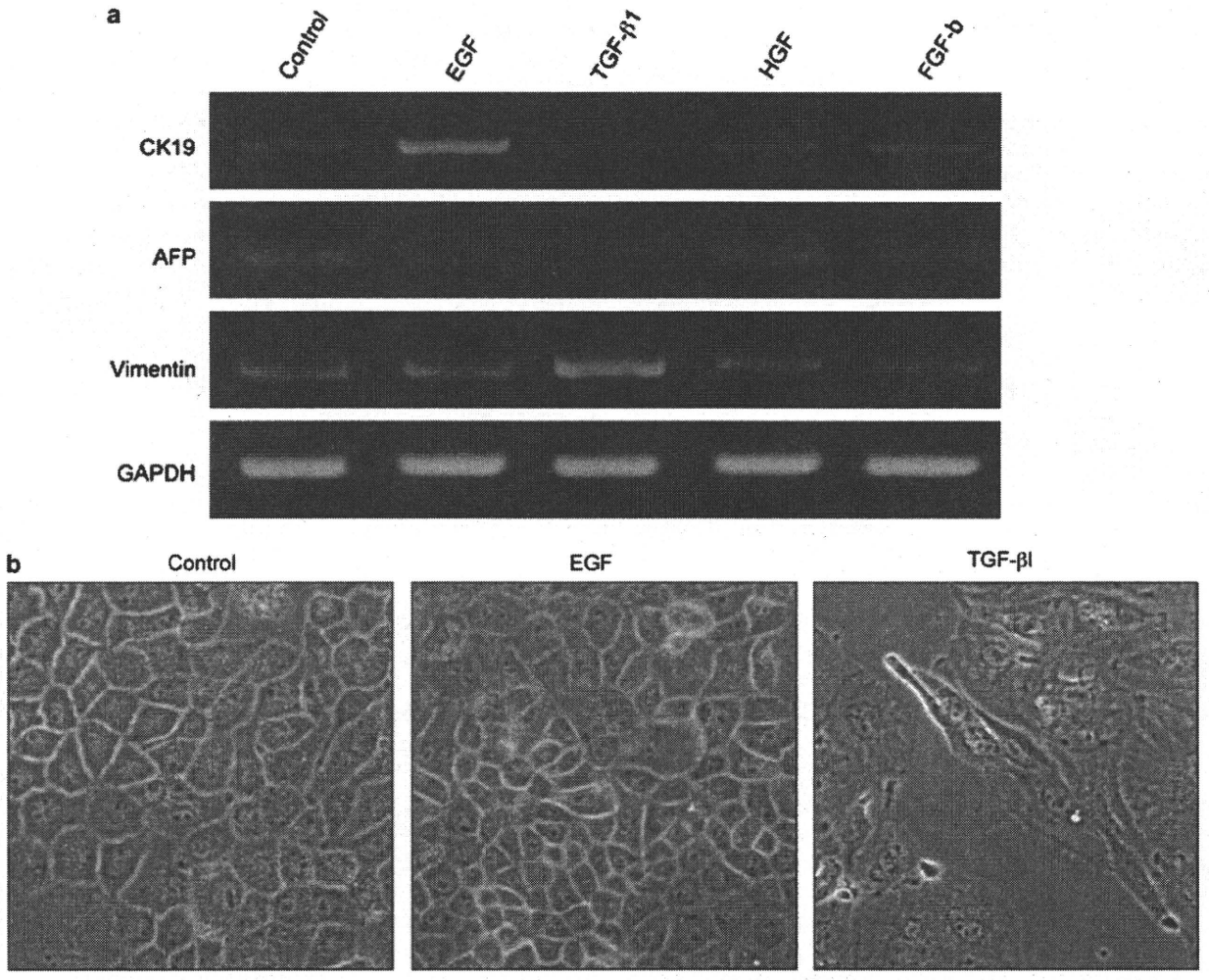

Figure 1 Expression analysis of CK19 mRNA after growth factor stimulation in HCC cell line. A human HCC cell line PLC-5 was treated with EGF, TGF-β1, HGF and FGF-b, and the mRNA expression of CK19, AFP and vimentin was examined by RT-PCR (**a**). EGF had a prominent effect on the induction of CK19 mRNA, accompanied by the reduction of AFP mRNA. The mRNA expression of vimentin was induced by TGF-β1 stimulation. On phase-contrast microscope, no morphological alteration was observed after treatment with EGF, whereas TGF-β1 induced spindle cell morphology (**b**). Original magnifications, x200 (**b**).

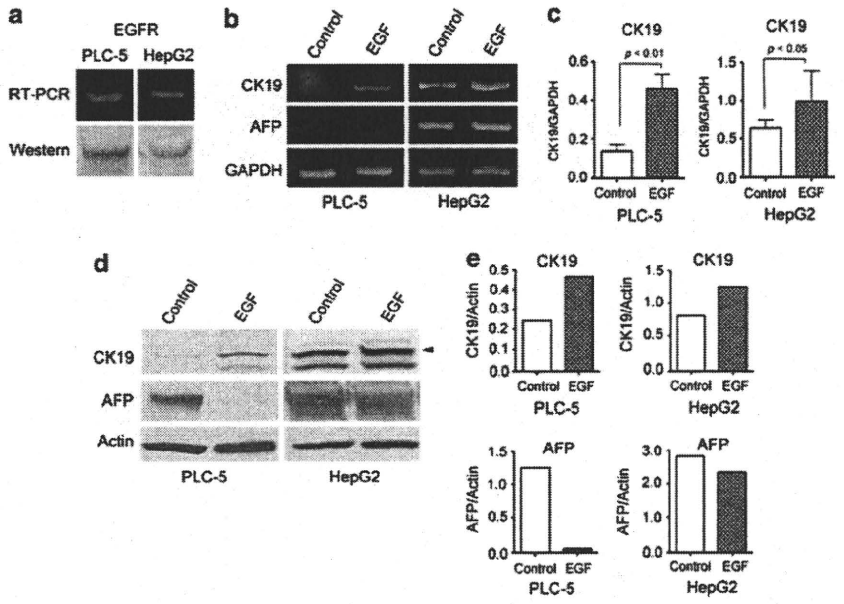

Figure 2 Induction of CK19 expression in HCC cell lines EGF stimulation. Two human HCC cell lines, PLC-5 and HepG2, expressed EGFR at the mRNA and protein levels (**a**). Stimulation of the cells with EGF induced CK19 mRNA expression, which was examined using RT-PCR (**b**) and real-time PCR (**c**). Western blot analysis showed the induction of CK19 protein in PLC-5 and HepG2 following EGF treatment (**d**), and semiquantitative analysis of the results confirmed this tendency (**e**). EGF reduced the expression of AFP in PLC-5 at the mRNA and protein levels, but their expression was unaffected in HepG2 (**b**, **d**, **e**). The data were expressed as the mean ± s.d. of six (**c**), and the mean of two sets (**e**).

Induction Of CK19 Expression In HCC Cell Lines By EGF

RT-PCR and western blot analysis confirmed that both PLC-5 and HepG2 expressed EGFR at the mRNA and protein levels (Figure 2a). EGF induced CK19 mRNA expression as assessed by RT-PCR (Figure 2b), and the results of real-time PCR confirmed that EGF significantly induced CK19 mRNA expression in both cell lines (Figure 2c). Western blot analysis also showed the induction of the expression of CK19 protein after EGF treatment in both cell lines (Figures 2d and 2e). EGF dramatically reduced the expression of AFP in PLC-5 at the mRNA and protein levels, but its expression was unaffected in HepG2 (Figures 2b, d and e).

Immunofluorescence staining of CK19 and AFP demonstrated that PLC-5 diffusely expressed AFP in their cytoplasm, whereas smaller number of cells showed positive immunoreactivity of CK19 in the control (no EGF treatment) group (Figure 3). After EGF treatment, most of the cells were strongly positive for CK19, and the expression of AFP was markedly reduced (Figure 3), which were consistent with the results of real-time PCR and western blotting.

Phosphorylation Of JNK/SAPK In HCC Cell Lines after EGF Stimulation

To determine the intracellular signaling pathway involved in the induction of CK19 expression, the expression of the phosphorylated form of JNK/SAPK, p38 MAPK, ERK1/2 and Akt was examined using western blotting. In PLC-5 and HepG2, the levels of phospho-JNK/SAPK expression increased after EGF treatment (Figures 4a and b). By contrast, the expression of phospho-p38 MAPK, ERK1/2 and Akt was unaffected by the treatment in both cell lines (data not shown).

To further examine the involvement of JNK/SAPK in the induction of CK19 expression, PLC-5 was treated with JNK inhibitors (JNK inhibitor I, JNK inhibitor II) in combination with EGF, and the expression of CK19 was examined by western blottng. As shown in Figures 4c and d, both JNK inhibitors suppressed the EGF–meditated induction of CK19 expression, indicating that JNK/SAPK is a downstream regulator of CK19 expression via EGF-EGFR. In addition, the JNK inhibitors reversed the EGF-mediated reduction of AFP expression in PLC-5 (Figures 4c and d).

Increase in Proliferative Ability and Invasive Property of HCC Cell Lines by EGF

The WST1 cell proliferation assay showed that the proliferative ability of the cells was higher in the EGF-treated groups than that of the control group in both PLC-5 and HepG2 (Figure 5a). Invasive properties of PLC-5 and HepG2 also significantly increased after EGF treatment, which was determined using the invasion assay (Figure 5b). Representative images of the invasion assay are shown in Figure 5c.

Expression Of CK19, EGF, EGFR, and JNK in Human HCC Tissues

Positive immunoexpression of CK19 in human HCC tissues was observed in limited number of cases. In most of the

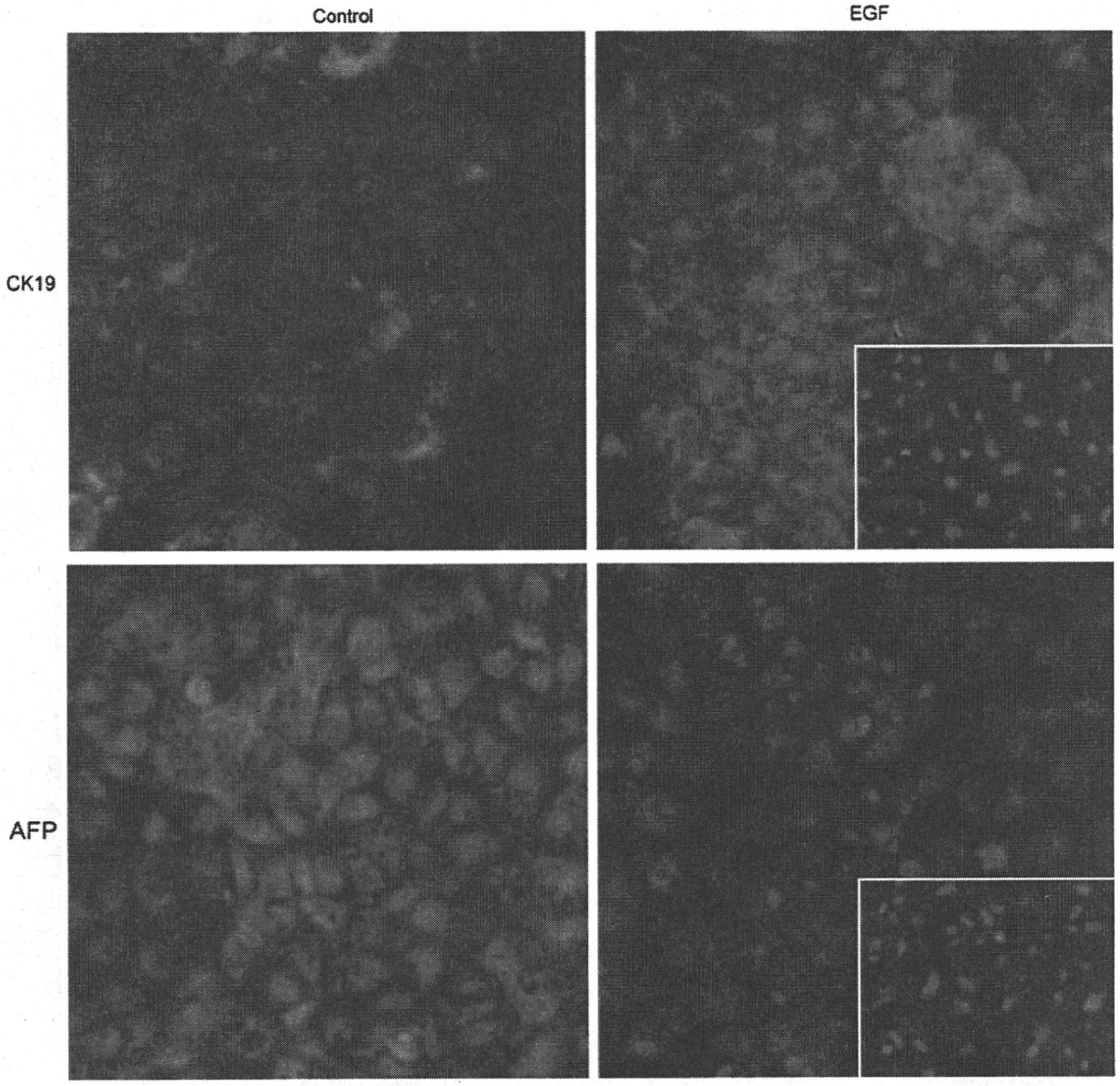

Figure 3 Alteration of CK19 and AFP expression in PLC-5 after EGF stimulation Immunofluorescence staining of CK19 and AFP was performed for PLC-5 with and without EGF treatment. CK19 and AFP were visualized by the Vector Red alkaline phosphatase substrate (red), and nuclei were stained with 4′6-diamino-2-phenylindole (blue). EGF markedly induced CK19 expression in PLC-5, and the expression of AFP was reduced. Negative controls for CK19 and AFP immunofluorescence staining were shown in the insets. Original magnifications, x200.

CK19-positive cases, CK19 expression in HCC was not diffusely observed, and CK19-positive cells were aggregated in focal areas in a single section (Figure 6b). On the basis of previous reports,[8,11,12] CK19-positive HCC was defined as such tumor that $<5\%$ of total carcinoma cells showed positive immunoreactivity of CK19 in this study. According to this definition, 9 (12%) of 78 cases of surgically resected HCC samples corresponded to CK19-positive HCC.

Immunohistochemical expression of EGF and EGFR in HCC varied from case to case (Figures 6c and d). Semi-quantitative analysis of the results of immunostaining showed that the positive immunohistochemical signals of EGF and EGFR were significantly more frequent in CK19-positive HCC compared with those of CK19-negative HCC ($P<0.01$ and $P<0.05$, respectively; Figure 6j). It is of note that all cases of CK19-positive HCC ($n=9$) showed positive immunohistochemical expression of EGF and EGFR (Figure 6j). Double immunostaining for CK19 and EGFR showed that EGFR was colocalized with CK19 (Figure 6e). *In situ* hybridization studies further

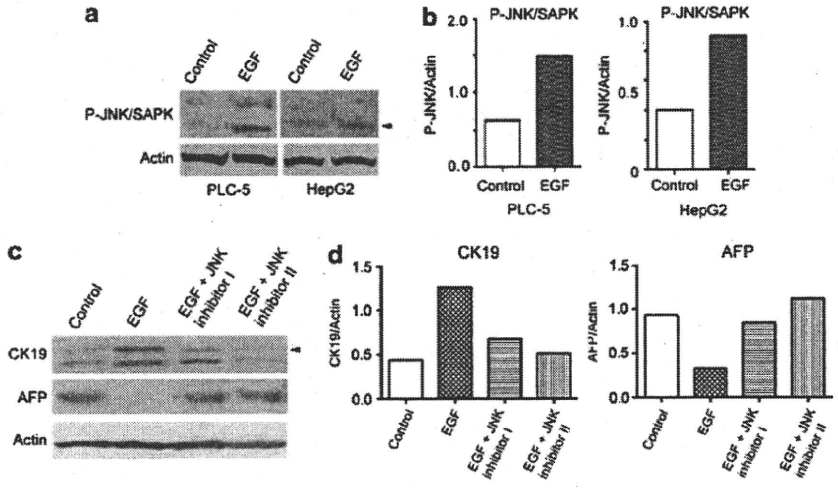

Figure 4 Phosphorylation of JNK/SAPK in HCC cell lines after EGF stimulation. Western blot analysis showed that the expression of phosphor-JNK/SAPK was increased in PLC-5 and HepG2 after EGF treatment (**a**). JNK inhibitor I and JNK inhibitor II blocked EGF-induced CK19 expression and EGF-induced AFP reduction in PLC-5 (**c**). The results of semiquantitative analysis of the western blotting were shown in (**b**) and (**d**). The data were expressed as the mean of two sets (**b**, **d**).

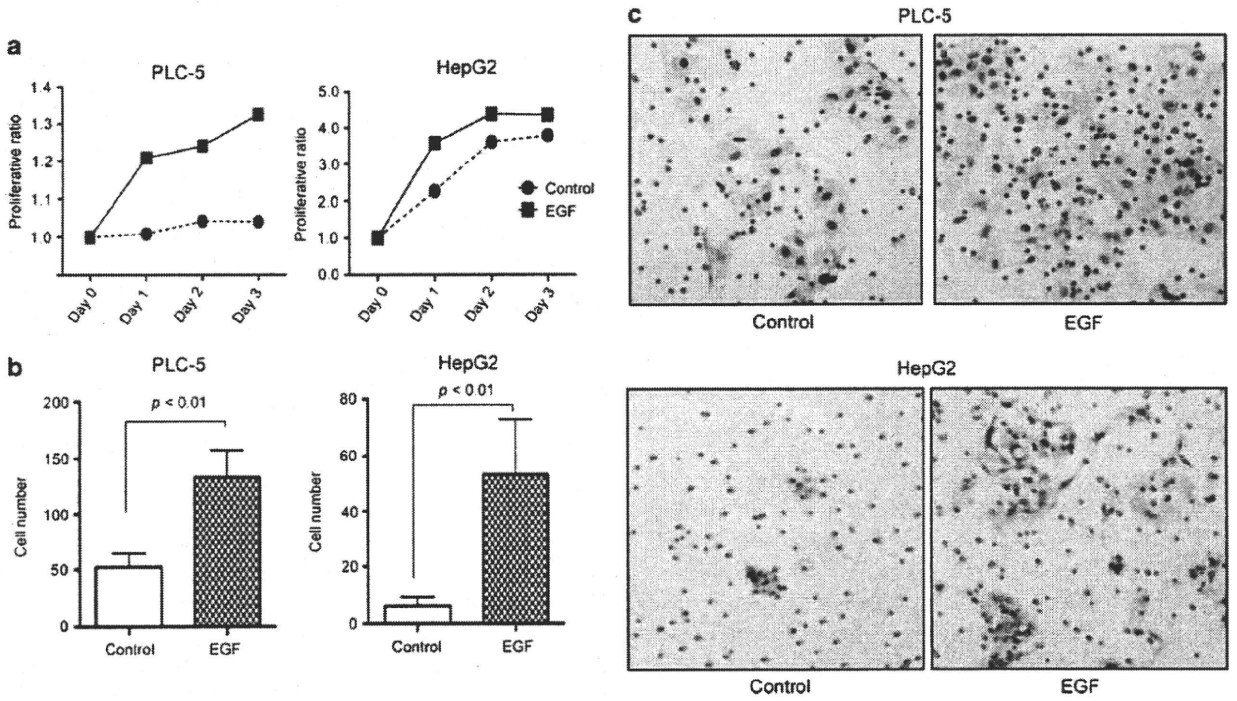

Figure 5 Increase in proliferative ability and invasive property of HCC cell lines by EGF. PLC-5 and HepG2 were treated with EGF, and the cell proliferative ability and invasive property were examined using the WST1 cell proliferation assay and the invasion assay, respectively. The cell proliferative ability was higher in EGF-treated group that that of control group in both PLC-5 and HepG2 (**a**). Invasive properties of PLC-5 and HepG2 was significantly increased after EGF treatment (**b**). Representative images of the invasion assay were shown in (**c**). Hematoxylin-stained blue nuclei indicate migrated cells (**c**). The data were expressed as the mean ± s.d. of five (**a**) and six sets (**b**). Original magnifications, x200 (**c**).

confirmed that CK19-positive HCC expressed EGFR mRNA (Figure 6f and g).

All cases of CK19-positve HCC showed immunohistochemical expression of JNK. Although the signal intensity of JNK was observed heterogeneously in a single section, it tended to be preferably expressed in the CK19-positive areas (Figure 6h and i; the lower part of the figures was CK19-positive area, and the upper part was CK-19-negative area). Semiquantitative analysis of the immunohistochemical expression of JNK showed that its expression was

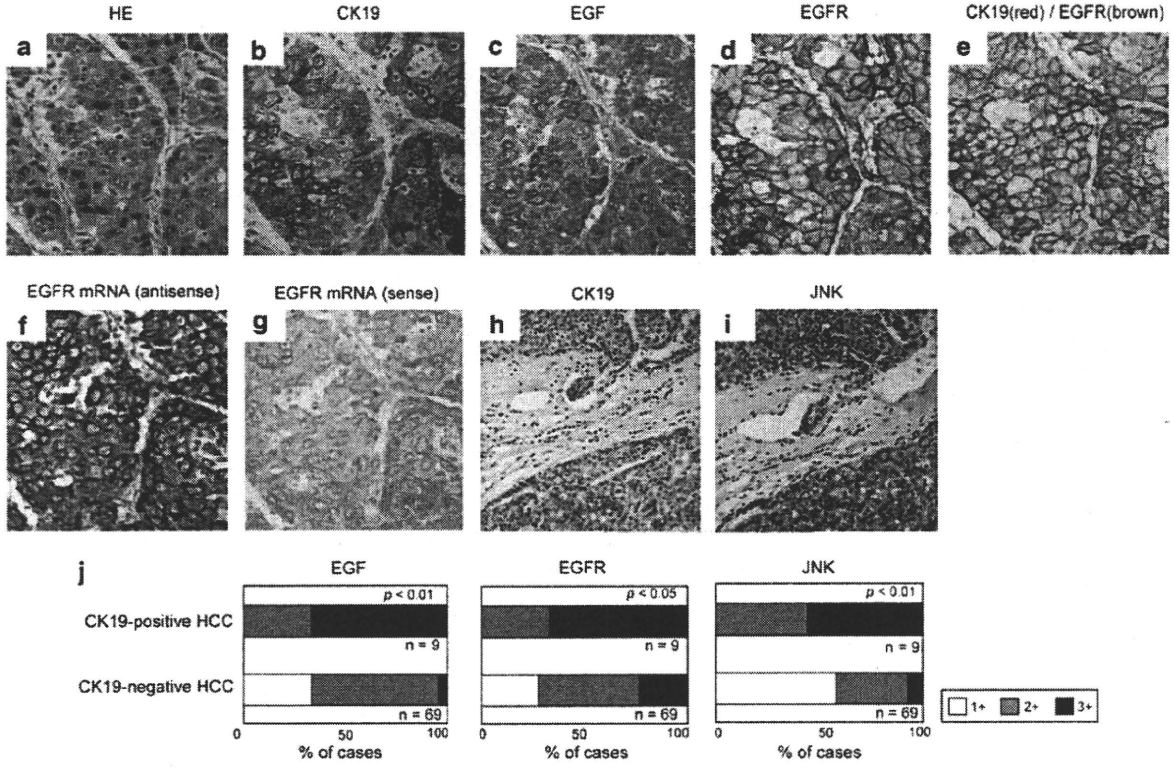

Figure 6 Expression of CK19, EGF, EGFR, and JNK in human HCC tissues. Examples of the results of histological analysis for one CK19-positive HCC case are shown (**a–i**). Carcinoma cells expressed CK19 (**b**), EGF (**c**) and EGFR (**d**). CK19 expression tended to be focal, and the expression of EGF and EGFR was diffuse in a single section. Double immunostaining of EGFR (brown) and CK19 (red) showed their colocalization (**e**). *In situ* hybridization studies confirmed that CK19-positive HCC expressed EGFR mRNA (**f, g**). The immunohistochemical expression of JNK was preferably observed in the CK19-positive areas (**h, i**; the lower part of the figures was CK19-positive area, and the upper part was CK-19-negative area). Semiquantitative analysis of the results of EGF, EGFR, and JNK immunostaining was performed as described in the Materials and Methods. The analysis showed that the extent of positive immunohistochemical signals of EGFR, EGF and JNK was significantly intense in CK19-positive HCC (**j**). Original magnifications; x400 (**a–g**), x100 (**h, i**).

significantly more frequent in CK19-positive HCC compared with that of CK19-negative HCC ($P<0.01$; Figure 6j).

Poor Prognosis of CK19-Positive HCC Patients

The results of clinicopathological analysis are summarized in Table 2. Portal vein invasion was observed more frequently in CK19-positive HCC compared with that of CK19-negative HCC, and there was a significant difference between them ($P=0.0348$). In addition, occurrence of extrahepatic metastasis after curative surgical hepatectomy was observed more frequently in CK19-positive HCC during the follow up period ($P=0.0085$). Extrahepatic metastasis was observed in three patients (43%) of CK19-positive HCC, in which two patients had bone metastasis, and one had adrenal metastasis. Other clinicopathlogical factors listed in Table 2 did not correlate significantly with CK19 expression in HCC.

In the whole study population, the 5-year disease free survival (DFS) and overall survival (OS) rates were 25.4 and 85.4%, respectively. CK19 positivity significantly correlated with the 2-year DFS rate ($P=0.0171$; Figure 7a). Both 5-year DFS and OS rates tended to be lower in CK19-positive HCC group, but CK19 positivity did not significantly correlated with the 5-year DFS rate ($P=0.0894$) and the 5-year OS rate ($P=0.6272$; Figures 7b and c).

DISCUSSION

This study demonstrated that EGF induced CK19 expression in well-established HCC cell lines, PLC-5 and HepG2, and revealed a possible mechanism underlying the development of CK19-positive HCC. In PLC-5, the induction of CK19 expression was accompanied by the marked reduction of AFP expression, indicating phenotypic transdifferentiation of the cells from hepatocellular-to-biliary phenotype.

In rat mature hepatocyte, transdifferentiation of hepatocyte to biliary epithelium has been demonstrated in experimental rodent models, hepatocyte organoid culture, and three-dimensional hepatocyte culture.[18–22] In these studies, EGF has been shown to be an essential promoter of the phenotypic transdifferentiation of mature hepatocytes.[18,20–22] This study demonstrated that EGF could induce phenotypic changes in HCC similar to those seen in non-cancerous mature hepatocytes. Previous studies also showed that HGF was another promoter of the phenotypic changes of mature hepatocytes.[18,21,22] However, as shown in Figure 1a, our

Table 2 Correlation between CK19 expression and clinicopathological factors in patients with hepatocellular carcinoma

	CK19 negative	CK19 positive	*P*-value
Patients	69	9	
Sex			
Male	57	7	0.7224
Female	12	2	
Age (mean)	67	60	0.1308
Virus			
HBV	7	1	0.9284
HCV	51	8	0.3249
Non-B non-C	11	0	0.1962
Preoperative AFP[a]			
>20	25	6	0.1729
<20	34	3	
Child-pugh score[b]			
A	54	7	0.8168
B	10	1	
TNM stage[c]			
I–II	53	8	0.7103
III–IV	10	1	
Portal vein invasion			
Positive	28	7	0.0348
Negative	41	2	
Tumor size			
>5 cm	14	2	0.8926
<5 cm	55	7	
Tumor number			
Multiple	13	2	0.8087
Single	56	7	
Encapsulation			
Positive	53	8	0.4091
Negative	16	1	
Histology			
Well	26	0	0.0579
Mod	41	9	
Por	2	0	
Extrahepatic metastasis[d]			
Positive	4	3	0.0085
Negative	46	4	

[a]A total of 10 patients did not have the available data.
[b]Six patients did not have the available data.
[c]Six patients did not have the available data.
[d]A total of21 patients did not have the available data.

preliminary studies failed to demonstrate significant changes in CK19 and AFP expression after HGF treatment in PLC-5.

The results of this study indicated that CK19 expression in HCC might be an acquired feature of the carcinoma cells once conventional HCC had arisen. Most carcinomas show phenotypic heterogeneity,[27] and CK19 expression in HCC is one of such examples. The heterogeneity may result from tumor cell renewal and adaptation to specific micro-environment. The presence of cancer stem cells may be another contributor of the heterogeneity.[28,29] The results obtained here may also be implicated in the histogenesis of combined hepatocellular cholangiocarcinoma; that is, the component of cholangiocarcinoma originates from the transdifferention of the HCC component, forming a combined hepatocellular cholangiocarcinoma that exhibits focal or diffuse immunohistochemical expression of CK19.[30,31]

The expression of EGFR has been observed in 40 to 70% of conventional HCC in previous studies.[32–35] A recent study showed that the expression of EGF was upregulated in advanced HCC compared with that of control liver tissue and early HCC.[36] In this study, all cases of human CK19-positive HCC were found to express EGFR and EGF, and double immunostainig showed that CK19 was colocalized with EGFR. These findings indicate that carcinoma cells produce EGF, and it acts with EGFR in an autocrine and/or paracrine manner, which in turn induces CK19 expression and thus forming CK19-positive HCC.

In this study, the expression of CK19 was seen in relatively limited number of cases of HCC, and not all cases that showed immunohistochemical expression of EGFR and EGF were CK19-positive HCC. As shown in Figure 4, *in vitro* studies indicated that the JNK/SAPK signaling pathway might have an important role in the CK19 induction of HCC. *In vivo*, the extent of the positive immunohistochemical expression of JNK tended to be more intense in the CK19-positive areas of HCC, and the JNK expression was observed more frequently in CK19-positive HCC. Therefore, the status of the expression of JNK may be one of the factors which account for the facts that all EGFR- and EGF-positive HCC did not express CK19. In addition, two HCC cell lines exhibited different responses to EGF *in vitro*; that is, the

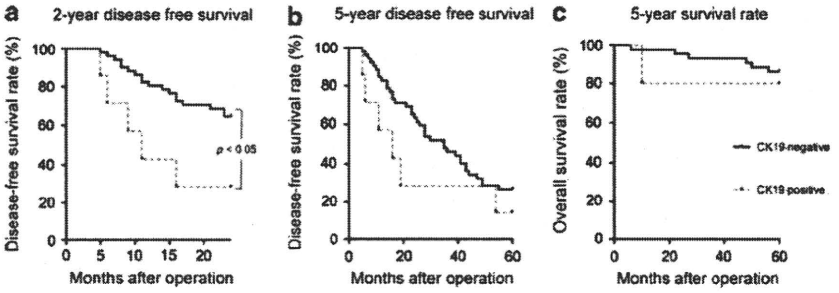

Figure 7 Poor prognosis of CK19-positive HCC patients. The correlation with the CK19 immunoreactivity and the DFS and OS rates were examined for 78 HCC patients. CK19 positivity significantly correlated with the 2-year DFS rate ($P = 0.0171$) (**a**). Both 5-year DFS rate (**b**) and OS rate (**c**) tended to be lower in CK19-positive HCC group, but CK19 positivity did not significantly correlated with the 5-year DFS rate ($P = 0.0894$) and the 5-year OS rate ($P = 0.6272$).

reduction of AFP expression occurred in PLC-5, whereas it did not reduced in HepG2, indicating complex intracellular signaling pathways involved in the EGF–EGFR axis in HCC.

In addition to the induction of CK19 expression, EGF increased proliferative abilities and invasive properties in PLC-5 and HepG2, demonstrating that stimulation with EGF led to more aggressive growth of HCC and increased malignant potential. These results were consistent with the findings of this study that CK19-positive HCC had a high incidence of portal vein invasion, extrahepatic metastasis, and an early relapse, which related to the worsened 2-year DFS rate.

The frequency of CK19-positive HCC was 12% (9/78 cases) in this study, and the frequency was almost consistent with previously reported data on the frequency of CK19-positive HCC (10–19%).[8,11,12] In accordance with these reports, CK19 positivity significantly correlated with the 2-year DFS rate.[8,11] Although the 5-year DFS and OS rate was not significantly correlated with CK19 positivity in this study, both of them tended to be lower in CK19-positive HCC group. Because this study dealt with relatively limited number of cases and the follow up periods were not sufficient, a significant difference might not be obtained.

In summary, this study elucidated an underlying mechanism of the development of CK19-positive HCC. The activation of the EGF–EGFR signaling pathway via phosphorylation of JNK/SAPK may be closely associated with the histogenesis of CK19-positive HCC. EGF increased the abilities of cell growth and invasive properties of HCC cell lines, showing an acquisition of more malignant potential and accounting for the poor prognosis of the patients. This study also confirmed previously reported findings that CK19-positive HCC had a poor prognosis. These results suggest that the inhibition of EGF–EGFR axis may improve the poor prognosis of the patients of CK19-positive HCC, implying as a potential therapeutic target.

DISCLOSURE/CONFLICT OF INTEREST

The authors declare no conflict of interest.

1. Parkin D. Global cancer statistics in the year 2000. Lancet Oncol 2001;2:533–543.
2. Jemal A, Siegel R, Ward E, *et al*. Cancer statistics. CA Cancer J Clin 2007;57:43–66.
3. Tang Z, Ye S, Liu Y, *et al*. A decade's studies on metastasis of hepatocellular carcinoma. J Cancer Res Clin Oncol 2004;130:187–196.
4. Yang Y, Nagano H, Ota H, *et al*. Patterns and clinicopathologic features of extrahepatic recurrence of hepatocellular carcinoma after curative resection. Surgery 2007;141:196–202.
5. Van Eyken P, Sciot R, Paterson A, *et al*. Cytokeratin expression in hepatocellular carcinoma: an immunohistochemical study. Hum Pathol 1988;19:562–568.
6. Robrechts C, De Vos R, Van den Heuvel M, *et al*. Primary liver tumour of intermediate (hepatocyte-bile duct cell) phenotype: a progenitor cell tumour? Liver 1998;18:288–293.
7. Yoon D, Jeong J, Park Y, *et al*. Expression of biliary antigen and its clinical significance in hepatocellular carcinoma. Yonsei Med J 1999;40:472–477.
8. Uenishi T, Kubo S, Yamamoto T, *et al*. Cytokeratin 19 expression in hepatocellular carcinoma predicts early postoperative recurrence. Cancer Sci 2003;94:851–857.
9. Wu P, Fang J, Lau V, *et al*. Classification of hepatocellular carcinoma according to hepatocellular and biliary differentiation markers. Clinical and biological implications. Am J Pathol 1996;149:1167–1175.
10. Ding S, Li Y, Tan Y, *et al*. From proteomic analysis to clinical significance: overexpression of cytokeratin 19 correlates with hepatocellular carcinoma metastasis. Mol Cell Proteomics 2004;3:73–81.
11. Yang X, Xu Y, Shi G, *et al*. Cytokeratin 10 and cytokeratin 19: predictive markers for poor prognosis in hepatocellular carcinoma patients after curative resection. Clin Cancer Res 2008;14:3850–3859.
12. Durnez A, Verslype C, Nevens F, *et al*. The clinicopathological and prognostic relevance of cytokeratin 7 and 19 expression in hepatocellular carcinoma. A possible progenitor cell origin. Histopathology 2006;49:138–151.
13. Moll R, Franke W, Schiller D, *et al*. The catalog of human cytokeratins: patterns of expression in normal epithelia, tumors and cultured cells. Cell 1982;31:11–24.
14. Osborn M, van Lessen G, Weber K, *et al*. Differential diagnosis of gastrointestinal carcinomas by using monoclonal antibodies specific for individual keratin polypeptides. Lab Invest 1986;55:497–504.
15. van Eyken P, Sciot R, van Damme B, *et al*. Keratin immunohistochemistry in normal human liver. Cytokeratin pattern of hepatocytes, bile ducts and acinar gradient. Virchows Arch A Pathol Anat Histopathol 1987;412:63–72.
16. Lai Y, Thung S, Gerber M, *et al*. Expression of cytokeratins in normal and diseased livers and in primary liver carcinomas. Arch Pathol Lab Med 1989;113:134–138.
17. Roskams T, De Vos R, Van Eyken P, *et al*. Hepatic OV-6 expression in human liver disease and rat experiments: evidence for hepatic progenitor cells in man. J Hepatol 1998;29:455–463.
18. Limaye P, Bowen W, Orr A, *et al*. Mechanisms of hepatocyte growth factor-mediated and epidermal growth factor-mediated signaling in transdifferentiation of rat hepatocytes to biliary epithelium. Hepatology 2008;47:1702–1713.
19. Michalopoulos G, Barua L, Bowen W. Transdifferentiation of rat hepatocytes into biliary cells after bile duct ligation and toxic biliary injury. Hepatology 2005;41:535–544.
20. Nishikawa Y, Doi Y, Watanabe H, *et al*. Transdifferentiation of mature rat hepatocytes into bile duct-like cells *in vitro*. Am J Pathol 2005;166:1077–1088.

21. Michalopoulos G, Bowen W, Mulé K, *et al.* Hepatocytes undergo phenotypic transformation to biliary epithelium in organoid cultures. Hepatology 2002;36:278–283.
22. Michalopoulos G, Bowen W, Mulé K, *et al.* Histological organization in hepatocyte organoid cultures. Am J Pathol 2001;159:1877–1887.
23. Del Castillo G, Alvarez-Barrientos A, Carmona-Cuenca I, *et al.* Isolation and characterization of a putative liver progenitor population after treatment of fetal pat hepatocytes with TGF-beta. J Cell Physiol 2008;215:846–855.
24. Yoshida M, Nishikawa Y, Omori Y, *et al.* Involvement of signaling of VEGF and TGF-beta in differentiation of sinusoidal endothelial cells during culture of fetal rat liver cells. Cell Tissue Res 2007;329: 273–282.
25. Xu C, Rosler E, Jiang J, *et al.* Basic fibroblast growth factor supports undifferentiated human embryonic stem cell growth without conditioned medium. Stem Cells 2005;23:315–323.
26. Zaret K. Hepatocyte differentiation: from the endoderm and beyond. Curr Opin Genet Dev 2001;11:568–574.
27. Heppner G. Tumor heterogeneity. Cancer Res 1984;44:2259–2265.
28. Vermeulen L, Sprick M, Kemper K, *et al.* Cancer stem cells—old concepts, new insights. Cell Death Differ 2008;15:947–958.
29. Bioulac-Sage P, Balabaud C, Wanless I. Diagnosis of focal nodular hyperplasia: not so easy. Am J Surg Pathol 2001;25:1322–1325.
30. Zhang F, Chen X, Zhang W, *et al.* Combined hepatocellular cholangiocarcinoma originating from hepatic progenitor cells: immunohistochemical and double-fluorescence immunostaining evidence. Histopathology 2008;52:224–232.
31. Aishima S, Nishihara Y, Kuroda Y, *et al.* Histologic characteristics and prognostic significance in small hepatocellular carcinoma with biliary differentiation: subdivision and comparison with ordinary hepatocellular carcinoma. Am J Surg Pathol 2007;31:783–791.
32. Buckley A, Burgart L, Sahai V, *et al.* Epidermal growth factor receptor expression and gene copy number in conventional hepatocellular carcinoma. Am J Clin Pathol 2008;129:245–251.
33. Tang Z, Qin L, Wang X, *et al.* Alterations of oncogenes, tumor suppressor genes and growth factors in hepatocellular carcinoma: with relation to tumor size and invasiveness. Chin Med J (Engl) 1998;111:313–318.
34. El-Bassiouni A, Nosseir M, Zoheiry M, *et al.* Immunohistochemical expression of CD95 (Fas), c-myc and epidermal growth factor receptor in hepatitis C virus infection, cirrhotic liver disease and hepatocellular carcinoma. APMIS 2006;114:420–427.
35. Ito Y, Takeda T, Sasaki Y, *et al.* Expression and clinical significance of the erbB family in intrahepatic cholangiocellular carcinoma. Pathol Res Pract 2001;197:95–100.
36. Villanueva A, Chiang D, Newell P, *et al.* Pivotal role of mTOR signaling in hepatocellular carcinoma. Gastroenterology 2008;135:1972–1983.

European Journal of Radiology xxx (2010) xxx–xxx

Contents lists available at ScienceDirect

European Journal of Radiology

journal homepage: www.elsevier.com/locate/ejrad

Detection of small hypervascular hepatocellular carcinomas by EASL criteria: Comparison with double-phase CT during hepatic arteriography

Olga Pugacheva[a], Osamu Matsui[b,*], Kazuto Kozaka[b], Tetsuya Minami[b], Yasuji Ryu[b], Wataru Koda[b], Satoshi Kobayashi[b], Toshifumi Gabata[b]

[a] Radiology Department, A.V. Vishnevsky Institute of Surgery, Bol. Serpukhovskaya Street, 27, Moscow 115093, Russia
[b] Department of Imaging Diagnosis and Interventional Radiology, Kanazawa University Graduate School of Medical Science, Kanazawa, 13-1 Takara-machi, 920-8641, Japan

ARTICLE INFO

Article history:
Received 11 June 2010
Received in revised form 19 August 2010
Accepted 26 August 2010

Key words:
Hepatocellular carcinoma
CTHA
CTAP
CT
MRI

ABSTRACT

Background and aims: To compare the detectability of small hypervascular hepatocellular carcinoma (HCC) between double-phase CT during hepatic arteriography (CTHA) criteria (hypervascular on the early-phase of CTHA and corona enhancement on the late-phase of CTHA) widely introduced in Japan and EASL criteria (hypervascular on the arterial dominant phase and wash out on the equilibrium phase of dynamic CT and/or MRI).
Methods: 116 hypervascular HCC lesions (≤2 cm) of 38 patients were evaluated. CTHA was performed in every patient, both dynamic CT and dynamic MRI in 22 patients, only dynamic CT in 8, and only dynamic MRI in 8. Among them, the detectability of HCC lesions was statistically analyzed with χ^2 test.
Results: Double-phase CTHA detected all HCCs. Dynamic CT revealed 38 (40%) of 95 small HCCs; during dynamic MRI 38 (40%) of 95 small HCCs were detected. The difference between dynamic CT or dynamic MRI and CTHA was statistically significant ($p < 0.05$).
Conclusion: The detectability of small hypervascular HCC on dynamic CT and dynamic MRI was almost the same and significantly lower as compared to that of CTHA. When comparing differences in the results of HCC treatment, differences in the diagnostic criteria applied should always be kept in mind.

1. Introduction

Hepatocellular carcinoma (HCC) is the most common primary malignant tumor of the liver and the 6th most common cancer worldwide [1]. HCCs most frequently occur in cirrhotic liver. Therefore, early detection and diagnosis of small HCCs in cirrhotic patients are very important to facilitate effective treatment and reduce mortality. In addition, the detection of small hypervascular intrahepatic metastasis and/or multicentric small hypervascular HCCs is indispensable for pre-treatment staging to improve the prognosis of patients with HCC, because the nature of hypervascular HCC is much more aggressive than that of hypovascular well differentiated HCC.

In Japan, angiography assisted CT including CT during arterial portography (CTAP) and CT during hepatic arteriography (CTHA) are widely performed as the most sensitive modality to detect hypervascular HCC [2–8]. However, in Europe and the United States, the imaging diagnosis of HCC is done only by contrast ultrasound, dynamic CT and MRI according to EASL (the European Association for the Study of the Liver) [9] or AASLD (the American Association for the Study of Liver Disease) criteria [10]. Because of these differences in imaging modalities and criteria, an important bias is likely to exist in the treatment results of HCCs reported from different countries or regions.

The purpose of this study was to retrospectively evaluate the detectability of small hypervascular HCC by dynamic CT and/or MR imaging based on EASL criteria in comparison with double-phase CT during hepatic arteriography (CTHA) widely performed in Japan and to discuss the differences in the staging of HCC among different diagnostic criteria or countries.

2. Materials and methods

2.1. Patients and hypervascular HCC nodules

Institutional review board approval for this type of retrospective study was not required at our institution. Written informed consent was obtained from each patient before the procedures. Successive

* Corresponding author. Tel.: +81 76 265 2323, fax: +81 76 234 4256.
E-mail addresses: PugachovaOlga@yandex.ru (O. Pugacheva), Matsuio@med.kanazawa-u.ac.jp (O. Matsui), k-kozaka@staff.kanazawa-u.ac.jp (K. Kozaka), tminami@staff.kanazawa-u.ac.jp (T. Minami), yryu-kanazawa@umin.ac.jp (Y. Ryu), wkoda@staff.kanazawa-u.ac.jp (W. Koda), satoshik@staff.kanazawa-u.ac.jp (S. Kobayashi), gabata@med.kanazawa-u.ac.jp (T. Gabata).

0720-048X/$ – see front matter © 2010 Elsevier Ireland Ltd. All rights reserved.
doi:10.1016/j.ejrad.2010.08.036

Please cite this article in press as: Pugacheva O, et al. Detection of small hypervascular hepatocellular carcinomas by EASL criteria: Comparison with double-phase CT during hepatic arteriography. Eur J Radiol (2010), doi:10.1016/j.ejrad.2010.08.036

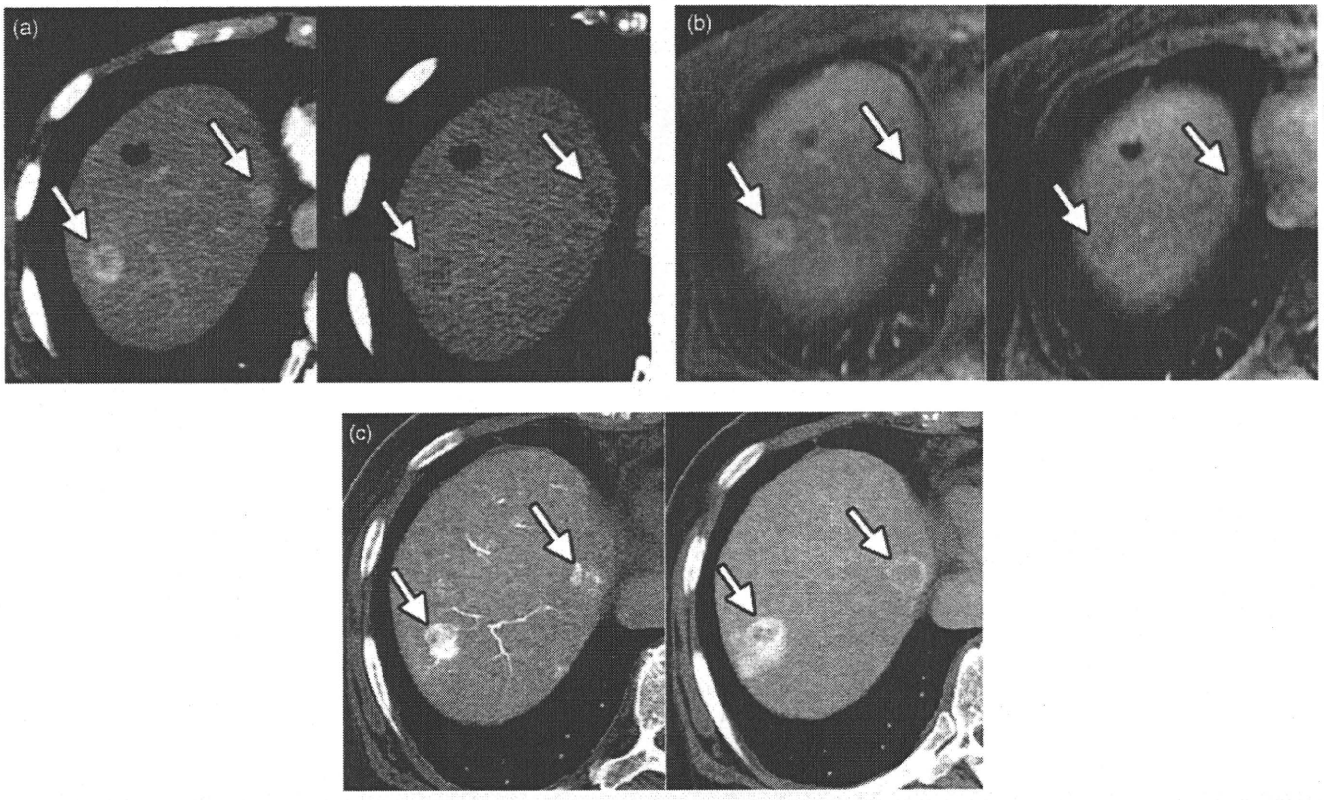

Fig. 1. A 74-year-old female with C-virus related chronic hepatitis with two hypervascular hepatocellular carcinomas (HCC) in S8 (19 mm) and S4 (11 mm). (A) Arterial dominant phase (left) of dynamic CT shows two enhanced nodules (arrows). On equilibrium phase (right), both of them demonstrate hypodensity indicating wash out of contrast medium. (B) On dynamic MRI, they show definite enhancement on arterial dominant phase (left, arrows) and wash out on equilibrium phase (right, arrows). (C) Early-phase of CT during hepatic arteriography (CTHA) reveal them as definitely hyperdense nodules (left, arrows) and they demonstrate wash out of contrast medium with surrounding corona enhancement on late-phase (right, arrows).

38 patients with HCC who underwent double-phase CTHA from September 2006 to March 2008 were subjected to the study. 26 men and 12 women with a mean age of 69.0 ± 8.7 years (range 48–83 years) were included. All patients had associated liver cirrhosis or chronic hepatitis, namely, chronic hepatitis C virus-related cirrhosis or chronic hepatitis in 31 patients, hepatitis B-virus related chronic hepatitis in 3, both hepatitis B and C virus-related cirrhosis in 1, alcoholic cirrhosis in 1 and cryptogenic fibrosis in 2. 24 patients had Child-Pugh class A, and 14 patients had Child-Pugh class B chronic liver disease.

In these 38 patients, small hypervascular HCCs with the greatest diameter ranged from 4 to 20 mm (mean diameter 11.1 ± 4.1 mm) confirmed by the following criteria were subjected to the analysis. The generally accepted imaging criteria of the imaging diagnosis of hypervascular HCC were hypervascularity relative to the surrounding liver on the arterial dominant phase and wash out on the equilibrium phase of dynamic CT and/or MRI (EASL criteria) (Fig. 1A and B) [9], and/or hypervascular nodule on the early-phase and corona enhancement on the late-phase of CTHA (CTHA criteria) (Fig. 1C) [4,6,7]. All measurements were performed on CTHA images. The final confirmation of the diagnosis was done based on the typical imaging features fulfilling both EASL and CTHA criteria. When the nodules fulfilled only either the EASL or CTHA criteria, the diagnosis of HCC was confirmed by one of the following: percutaneous biopsy, surgical resection, definite nodular accumulation of iodized oil (Lipiodol) more than one month after transcatheter arterial chemoembolization (TACE), or definite growth of the lesion during more than 1 year follow up. Hypovascular HCCs demonstrating no definite enhancement on CTHA were excluded from the study.

Among these HCC nodules, detectability of HCCs by dynamic CT and dynamic MRI based on the criteria of EASL were analyzed in comparison with double-phase CTHA.

2.2. Technique

All 38 patients underwent CTHA examination, dynamic CT was performed in 30, and dynamic MRI was performed in 30, and both in 22 patients. The time between the CTHA and dynamic CT and/or dynamic MRI examinations did not exceed 60 days to minimize the number of false-negative results because of the rapid growth of some HCC.

2.3. CTHA

CTHA was performed after hepatic angiography using a combined digital subtraction angiography (DFP 2000 A; Toshiba, Japan) and helical CT (X Vision SP; Toshiba Medical System, Tokyo, Japan) system. After femoral artery puncture, a 4-French catheter was selectively placed in the common or proper hepatic artery. Images were acquired through the liver in a craniocaudal direction with a 0.625 × 64 beam collimation. Other CT parameters were as follows: Auto mA (GE Healthcare; 10–700 mA, Noise Index of 8.0); 120 kVp; detector collimation, 2.5 mm; table speed, 14 mm per rotation; gantry rotation time, 0.5 s. CTHA scans were obtained at 3–5-mm section thickness and 3–5-mm collimation. Helical scanning was started 7 s after the beginning of an infusion of iohexol (320–350 mg of iodine per ml) (Omnipaque; Daiichi, Tokyo, Japan) into the common, proper hepatic artery at a rate of 1.8 ml/s. In the case of an anatomic variation, CTHA was performed via each right and left

Please cite this article in press as: Pugacheva O, et al. Detection of small hypervascular hepatocellular carcinomas by EASL criteria: Comparison with double-phase CT during hepatic arteriography. Eur J Radiol (2010), doi:10.1016/j.ejrad.2010.08.036

hepatic artery with an infusion of iohexol at a rate of 1.0–1.8 ml/s. The infusion of contrast material was continued until 5 s after early-phase CTHA scanning was completed. The scanning time varied according to the individual liver size (about 20–25 s). The total amount of contrast medium varied according to the following equation: (early-phase scanning time +12 s) × injection rate. Thirty seconds after completion of the contrast material infusion (about 50 s after the infusion began), late-phase scanning commenced.

2.4. Multidetector row CT

CT examinations were performed using a 64-detector row CT system (LightSpeed VCT, GE Medical System). Images were acquired through the liver in a craniocaudal direction with a 0.625 × 64 beam collimation. Other CT parameters were as follows: Auto mA (GE Healthcare; 10–700 mA, Noise Index of 8.0); 120 kVp; detector collimation, 2.5 mm; table speed, 14 mm per rotation; gantry rotation time, 0.5 s. A reconstruction section thickness of 2.5 mm and a reconstruction interval of 2.5 mm were used. Before the examinations, patients were instructed to hold their breath to avoid motion artifacts. Unenhanced multidetector row CT was performed first. For dynamic CT, contrast medium with a concentration of 320 mg of iodine per ml (iohexol, Omnipaque, Daiichi, Tokyo, Japan) was administered with a power injector. The total volume of 100 ml was injected at a rate of 3 ml/s through a 21-gauge plastic intravenous catheter that was placed in an antecubital vein. Thirty-five seconds after initiation of the injection, the early arterial phase CT acquisition began. The dynamic images consisted of three phases (i.e., arterial dominant, portal dominant and equilibrium phases). The equilibrium phase was scanned at 150 s after the injection of the contrast medium. In our analysis the arterial dominant and the equilibrium phases of dynamic CT were examined.

2.5. MR imaging

MR imaging was performed with a 1.5-T MR imaging unit (Signa Horizon; GE Medical Systems, Milwaukee, WI). All images were obtained in the transverse plane using a phased-array multicoil. The matrix size was 128 × 256 or 256 × 256. For dynamic imaging, gadopentetate dimeglumine (Magnevist; Schering, Berlin, Germany) was injected as a rapid bolus with a power injector at a dose of 0.1 mmol/kg and immediately followed by a 10–20 ml saline flush. The dynamic T1-weighted fast multiplanar spoiled gradient-recalled-echo (150/1.6, one acquisition, fat saturation) imaging examinations were performed with a flip angle of 90°, obtained in the transverse plane during suspended respiration immediately after intravenous injection of the gadolinium chelate, and additional images were obtained at 30–35 s (arterial dominant phase), 65–70 s (portal phase), and 3 min (equilibrium phase). In our analysis the arterial and equilibrium phases of dynamic MRI were used.

2.6. Image analysis

All images were reviewed on a PACS workstation, and the diameter of the lesion was measured with an electronic ruler.

All images of dynamic CT, dynamic MRI and CTHA were reviewed at the same time by two abdominal radiologists (O.P. and O.M., with 4 and 38 years of radiology experience respectively) and all lesions fulfilling EASL and/or CTHA criteria were picked up by consensus. Then, according to the above-mentioned criteria, the diagnosis of hypervascular HCC was confirmed in these lesions. All measurements of the diameter of the lesions were performed on CTHA images, and the largest diameter was employed for the analysis. Disagreements were resolved by consensus. Interobserver correlation was not analyzed because of the simplicity of image interpretation.

Table 1
Number of small hypervascular hepatocellular carcinomas (HCC) satisfied double-phase CT during hepatic arteriography (CTHA) criteria and EASL criteria on dynamic CT.

Size of HCCs[a] (n = 95)	Number of HCCs, satisfied CTHA criteria	Number of HCCs, satisfied EASL criteria
4–5 mm (n = 10)	10 (100%)	1 (10%)
6–10 mm (n = 39)	39 (100%)	12 (30.7%)
11–15 mm (n = 29)	29 (100%)	13 (44.8%)
16–20 mm (n = 17)	17 (100%)	12 (70.5%)

Abbreviation: HCC, hepatocellular carcinoma; EASL, the European Association for the Study of the Liver.
[a] Total number of HCCs satisfied CTHA and/or EASL criteria.

2.7. Statistical analysis

Statistical analysis was performed using χ^2 test for evaluating the association between the modalities and the detectability of the lesions. Differences were considered significant when the p value was less than 0.05. Statistical analyses were performed using a statistical software package (SPSS 11.0J for Windows; SPSS, Chicago, IL).

3. Results

A total of 59 nodular lesions fulfilling EASL and CTHA criteria were identified by two radiologists (O.P and O.M.) in 38 patients. All of the lesions fulfilling the EASL criteria on dynamic CT and/or MRI also revealed CTHA criteria definitely (Fig. 1), namely all lesions showed hypervascularity on the first phase of CTHA and corona enhancement on the late-phase of CTHA. On the other hand, no lesions fulfilling EASL criteria on dynamic CT or MRI without showing CTHA criteria were seen. In addition to these 59 hypervascular HCCs, 57 other lesions fulfilled only CTHA criteria and were finally confirmed as hypervascular HCC as follows: percutaneous biopsy in 19 lesions, surgical resection in 2 lesions, definite nodular accumulation of iodized oil (Lipiodol) more than one month after transcatheter arterial chemoembolization (TACE) in 23 lesions, and definite growth of the lesion during more than 1 year follow up in 13 lesions.

The sizes of these 116 HCC lesions were 4–20 mm (mean diameter 11.1 ± 4.1 mm); 11 HCCs had a diameter measuring 4–5 mm, 50 HCCs 6–10 mm, 35 HCCs 11–15 mm, and 20 HCCs 16–20 mm.

Dynamic CT was performed in 95 HCCs in 30 patients, and 38 of them (40%) demonstrated arterial enhancement on the arterial dominant phase and wash out on the equilibrium phase, thereby satisfying EASL criteria. Among 17 lesions with a diameter of 16–20 mm (mean diameter 17.5 ± 1.7 mm), 12 lesions (70.5%) satisfied EASL criteria (Fig. 1), and 3 lesions were visualized only in the arterial dominant phase. Among 29 lesions with a diameter of 11–15 mm (mean diameter 13.1 ± 1.6 mm), 13 lesions (44.8%) satisfied EASL criteria, and 6 lesions were visualized only in the arterial dominant phase. Among 39 lesions with a diameter of 6–10 mm (mean diameter 8.6 ± 1.4 mm), 12 HCCs (30.7%) satisfied EASL criteria (Fig. 1), and 7 lesions were depicted only on the arterial dominant phase as a hypervascular nodule. Among 10 lesions with a diameter of 4–5 mm (mean diameter 4.6 ± 0.5 mm), only one lesion (10%) fulfilled the EASL criteria and one lesion showed hypervascularity on the arterial dominant phase without wash out in the equilibrium phase (Fig. 2 and Table 1). Other lesions were not depicted on either the arterial dominant or equilibrium phases of dynamic CT (Fig. 3).

Dynamic MRI was performed in 95 HCCs in 30 patients, with 38 of them (40%) satisfying EASL criteria. Thirteen of 17 lesions (76.4%) with a diameter of 16–20 mm satisfied EASL criteria (Fig. 1), and 3 lesions were depicted as hypervascular nodules on the arterial

Please cite this article in press as: Pugacheva O, et al. Detection of small hypervascular hepatocellular carcinomas by EASL criteria: Comparison with double-phase CT during hepatic arteriography. Eur J Radiol (2010), doi:10.1016/j.ejrad.2010.08.036

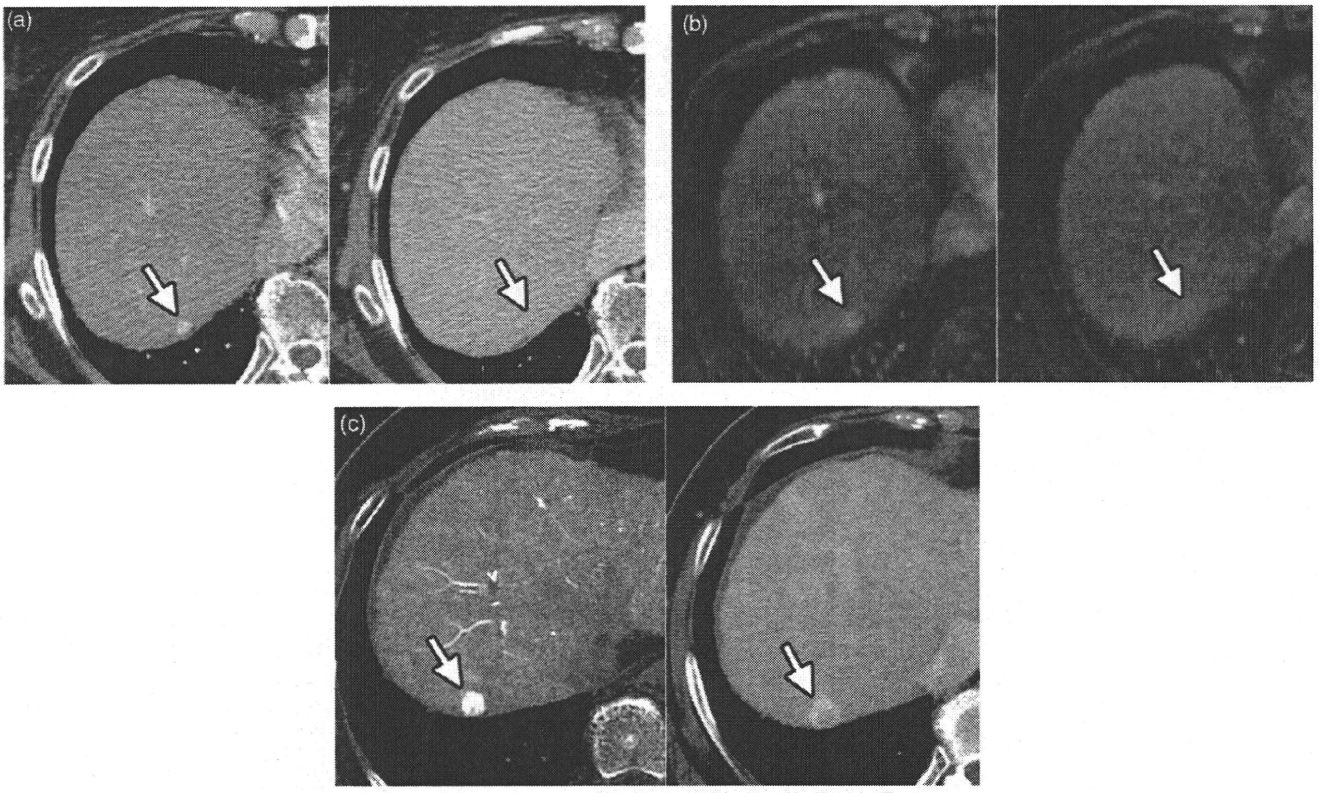

Fig. 2. A 73-year-old female with C-virus related liver cirrhosis with multiple small hypervascular HCCs. (A) Arterial dominant phase of dynamic CT shows a tiny hypervascular nodule around 4 mm in diameter at S7 (left, arrow). It cannot be identified on equilibrium phase (right, arrow). (B) It also shows nodular enhancement on arterial dominant phase of dynamic MRI (left, arrow) without showing wash out on equilibrium phase (right, arrow). (C) Early-phase of CTHA clearly demonstrates it as hypervascular nodule (left, arrow), and it is depicted as a slightly hypodense nodule with surrounding corona enhancement (wash out) on late-phase (right, arrow).

dominant phase without wash out in the equilibrium phase. Thirteen of 30 HCCs with a diameter of 11–15 mm (43.3%) satisfied EASL criteria, and 9 lesions were visualized as enhanced nodules in the arterial dominant phase without wash out in the equilibrium phase. Eleven of 41 HCCs (26.8%) with a diameter of 6–10 mm, satisfied EASL criteria (Fig. 1), and 10 lesions were depicted as enhanced nodules on the arterial dominant phase without wash out in the equilibrium phase. Only one of 7 HCCs (14%) with a diameter of 4–5 mm satisfied EASL or AASLD criteria, and 2 lesions showed enhancement on the arterial phase without wash out in the equilibrium phase (Fig. 2). Other lesions were not depicted on either the arterial dominant or equilibrium phases of dynamic MRI (Fig. 4 and Table 2).

Table 2
Number of small hypervascular hepatocellular carcinomas (HCC) satisfied double-phase CT during hepatic arteriography (CTHA) criteria and/or EASL criteria on dynamic MRI.

Size of HCCs[a] (n = 95)	Number of HCCs, satisfied CTHA criteria	Number of HCCs, satisfied EASL criteria
4–5 mm (n = 7)	7 (100%)	1 (14%)
6–10 mm (n = 41)	41 (100%)	11 (26.8%)
11–15 mm (n = 30)	30 (100%)	13 (43.3%)
16–20 mm (n = 17)	17 (100%)	13 (76.4%)

Abbreviation: HCC, hepatocellular carcinoma; EASL, the European Association for the Study of the Liver.

[a] Total number of HCCs satisfied CTHA and/or EASL criteria.

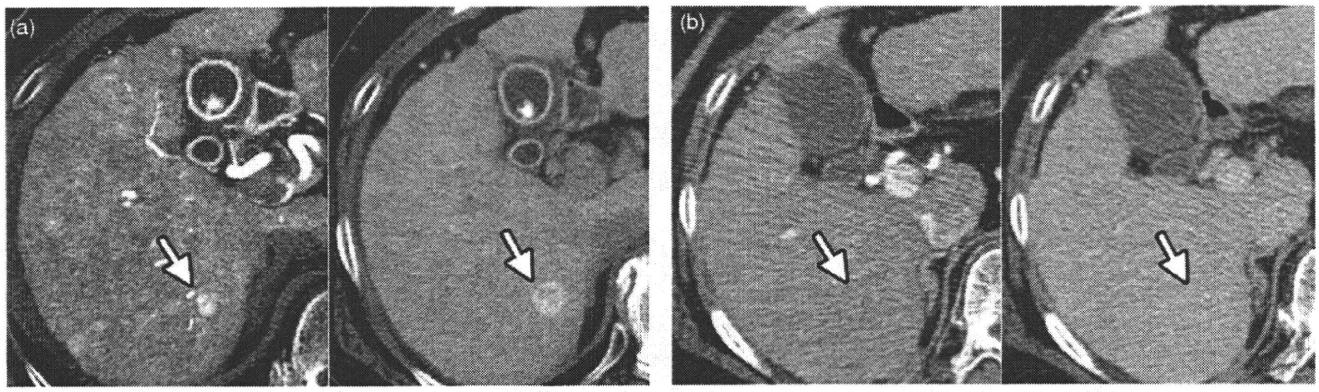

Fig. 3. A 73-year-old female with C-virus related liver cirrhosis with multiple small hypervascular HCCs (the same patient as in Fig. 2). (A) Double-phase CTHA demonstrates a nodule around 9 mm in diameter in S7 showing definite hypervascularity on early-phase (left, arrow) and corona enhancement indicating wash out on late-phase (right, arrow). (B) This lesion cannot be identified on either arterial dominant (left) or equilibrium (right) phases of dynamic CT.

Please cite this article in press as: Pugacheva O, et al. Detection of small hypervascular hepatocellular carcinomas by EASL criteria: Comparison with double-phase CT during hepatic arteriography. Eur J Radiol (2010), doi:10.1016/j.ejrad.2010.08.036

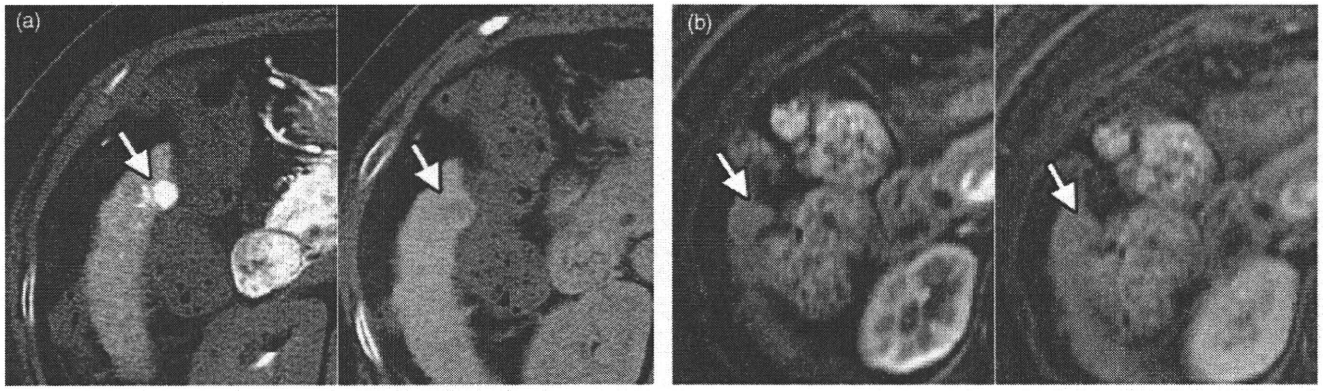

Fig. 4. A 73-year-old female with C-virus related liver cirrhosis with multiple small hypervascular HCCs (the same patient as in Fig. 2). (A) Double-phase CTHA demonstrates a nodule around 11 mm in diameter in S6 showing definite hypervascularity on early-phase (left, arrow) and wash out on late-phase (right, arrow). (B) This lesion cannot be identified on either arterial dominant (left) or equilibrium (right) phases of dynamic MRI.

In 74 HCCs in 22 patients, both dynamic CT and MRI were carried out. Among them, both CT and MRI fulfilled EASL criteria only in 16 lesions (21.6%).

The detectability of small hypervascular HCC was significantly lower on dynamic CT or dynamic MRI than in double-phase CTHA ($p < 0.05$). There was no significant difference in the detectability between dynamic CT and MRI.

4. Discussion

Detection of early stage small HCC and/or small intrahepatic metastasis of HCC by imaging is important clinically both to help long-term survival of patients with cirrhosis and to precisely stage HCC pre-treatment. However, the diagnostic ability of each imaging modality for HCCs is different and their availability is variable in different countries and/or regions because of different economic background, insurance systems, and other socioeconomic issues. Accordingly, all guidelines recommend performing screening and staging for HCC under their own diagnostic criteria using specific imaging modalities [10]. Among these criteria, EASL and/or AASLD criteria are now commonly employed worldwide [8,9]. However, in Japan, angiography assisted CT including CTAP and CTHA is accepted as an optional imaging modality for the precise evaluation of HCC in the guidelines proposed by the Japan Society of Hepatology [11] and widely performed at major Japanese institutions using a combined CT and digital angiography system. Therefore, some important bias may be introduced when we compare the previously reported treatment results of HCCs from different countries using different diagnostic modalities or criteria.

In Europe and the USA, the diagnosis of HCC is made only by contrast ultrasound, dynamic CT and MRI according to EASL or AASLD criteria. By these criteria, it is possible to establish an HCC diagnosis if a nodule within a cirrhotic liver exhibits intense arterial uptake followed by contrast wash out in the equilibrium (or late) phase. Trying to prevent false-negative HCC diagnosis in tiny lesions, it was recommended that in nodules between 1 and 2 cm, the diagnosis should require the consistent findings of two techniques [8,9]. In the study of Forner et al. [10] concerning prospective validation of the noninvasive diagnostic criteria for HCC less than 20 mm in the largest diameter confirmed by these particular criteria or biopsy, the diagnostic ability of contrast ultrasound and dynamic MRI were 51.7% and 61.7% respectively. Sensitivity for consistent conclusive findings on both techniques was 33% [10]. Similar or poorer diagnostic accuracy of MDCT and MRI according to EASL criteria was reported in the diagnosis of HCCs in explanted livers [12,13].

We previously revealed the changes occurring in the drainage vessels during hepatocarcinogenesis by correlation studies of CTAP and CTHA findings with histology [4,14]. As the tumor cells become more atypical and proliferate more rapidly, they first invade the intranodular hepatic veins because they do not contain fibrous tissue (e.g., Glisson's sheath surrounding portal veins). In the perinodular area, hepatic veins are similarly collapsed by tumor compression. When the drainage through hepatic veins is blocked, the drainage blood from the tumor flows mainly into surrounding hepatic sinusoids and partially into portal veins according to the blood pressure gradient. As the intranodular cellular density increases, the tumor growth pattern changes from replacing growth to compressive growth, and a thick fibrous capsule is formed by the compressed perinodular liver tissue. At this stage, perinodular hepatic sinusoids are collapsed, and the continuity of intranodular and extranodular sinusoids is interrupted by fibrous capsule formation. Therefore, drainage blood flow has no outlet other than through portal veins, accompanied by a marked increase in the arterial blood supply. Although the total number of intranodular portal veins is decreased, portal venules are relatively well preserved in the fibrous septa and capsule. These patent portal venules can become the drainage vessels of an established encapsulated HCC [4]. Because of these drainage routes of the feeding arterial blood, corona-like peritumoral enhancement is always seen in the late-phase of CTHA in hypervascular HCCs [14]. This corona-like enhancement on late-phase CTHA is virtually diagnostic for HCC as verified by comparative studies in resected HCCs [4,6,7,15]. According to Murakami et al. [7], the positive predictive value of corona enhancement on late-phase of CTHA was near 100% in hypervascular HCCs more than 1 cm. As for the sensitivity, it may depend on the size and arterial vascularity of HCCs. When only hypervascular HCCs on dynamic CT or MRI are included in the analysis, as shown in this study, the sensitivity of corona enhancement on late-phase CTHA may be near 100% except for metastatic liver cancers [16] and hypervascular hyperplastic nodules in alcoholic cirrhotic livers [17]. However, there a few diagnostic limitations in double-phase CTHA. In some cases of well differentiated HCC with relatively low arterial vascularity, they may show slight hyperdensity on early-phase CTHA without corona enhancement on late-phase and the differentiation from hypervascular pseudolesions is difficult. In addition, the interstitial fibrous tissue surrounding a regenerative nodule may show ring enhancement mimicking corona-like enhancement resulting in false positive diagnosis of a minute HCC.

In our present study, all of 116 small hypervascular HCCs less than 2 cm were diagnosed by double-phase CTHA. On the other hand, there was no hypervascular HCC that could be diagnosed by dynamic CT or MRI under EASL criteria but not by double-phase CTHA. According to the EASL criteria, dynamic CT detected 40.0%

Please cite this article in press as: Pugacheva O, et al. Detection of small hypervascular hepatocellular carcinomas by EASL criteria: Comparison with double-phase CT during hepatic arteriography. Eur J Radiol (2010), doi:10.1016/j.ejrad.2010.08.036